

SOT



Technical Memorandum 79653

(NASA-TM-79653) INFERENCE OF THE BOUNDARY
LAYER STRUCTURE OVER THE OCEANS FROM
SATELLITE INFRARED MEASUREMENTS (NASA) 60 p
HC A04/NF A01

M81-21436

CSSL 04A

Unclass

G3/43 21028

Inference of the Boundary Layer Structure Over the Oceans from Satellite Infrared Measurements

C. Prabhakara, G. Dalu,
R. Lo and N. R. Nath

SEPTEMBER 1978



National Aeronautics and
Space Administration

Goddard Space Flight Center
Greenbelt, Maryland 20771

**INFERENCE OF THE BOUNDARY LAYER STRUCTURE OVER
THE OCEANS FROM SATELLITE INFRARED MEASUREMENTS**

C. Prabhakara, G. Dalu*

NASA/Goddard Space Flight Center

Greenbelt, Md. 20771

R. Lo, N. R. Nath

Computer Sciences Corporation

Silver Spring, Md. 20910

September 1978

***NAS/NRC Research Associate on leave from C.N.R., Istituto di Fisica della Atmosfera, Rome, Italy.**

GODDARD SPACE FLIGHT CENTER

Greenbelt, Maryland

CONTENTS

	<u>Page</u>
ABSTRACT	iii
INTRODUCTION	1
EXAMINATION OF THE INFORMATION CONTENT IN IRIS SPECTRA	2
THEORETICAL CONSIDERATIONS	6
SPECTRAL SIMULATIONS FOR DIFFERENT ATMOSPHERIC MODELS	8
OBSERVATIONS AND RESULTS	28
CONCLUSIONS	47
REFERENCES	49

TABLES

<u>Table</u>	<u>Page</u>
1 Mean profiles of relative humidity and temperature for different latitude belts and seasons (from Nieman, 1977)	10
2 Mean line strength $\bar{\ell}$ and total precipitable water \bar{w} as a function of the surface temperature T_s for different mean atmospheres	12
3 Three parameter representation of the trade wind inversion (based on Meteor data, see Figs. 7 and 8)	21
4 Computed $9\mu\text{m}$ line strength corresponding to three trade wind inversions (see Table 3) for tropics (a), mid-latitude summer (b), and mid-latitude winter (c)	24
5a Temperature and relative humidity profiles for observed cases of ITCZ	27
5b Calculated $9\mu\text{m}$ line strength, the total water content \bar{w} , and the index $(\bar{w} - w)/\bar{w}$ for the ITCZ cases	28
6a Coincident data from ship radiosonde stations and Nimbus 4 IRIS	36

PRECEDING PAGE BLANK NOT FILMED

FIGURES (Continued)

<u>Figure</u>	<u>Page</u>
10 Adopted mean relative humidity profile (shown also in Fig. 3) and the models of the relative humidity profile for three conditions (see Table 3) of the inversion	23
11 Relationship between the temperature increase ΔT , from bottom to top of the inversion and the index $(\bar{w} - w)/\bar{w}$ based on the data given in Table 4	26
12 Distribution of the 9 μm line strength over the global oceans (50°N to 40°S) derived from the Nimbus 4 IRIS data for the period April, May and June, 1970	30
13 Same as Fig. 12 but for the period July, August and September, 1970	31
14 Same as Fig. 12 but for the period October, November and December, 1970	32
15 Distribution of the surface temperature over the global oceans (50°N to 40°S) derived from the 11 μm window region observations of the Nimbus 4 IRIS for the period April, May and June, 1970	33
16 Same as Fig. 15 but for the period July, August and September, 1970	34
17 Same as Fig. 15 but for the period October, November and December, 1970	35
18 Comparison between the water vapor content derived from the 9 μm line strength and the water vapor content obtained from radiosonde data	38
19 Distribution of the total water vapor content (g/cm^2) over the global oceans (50°N to 40°S) derived from the Nimbus 4 IRIS data over the period April, May and June, 1970	39
20 Same as Fig. 19 but for the period July, August and September, 1970	40
21 Same as Fig. 19 but for the period October, November and December, 1970	41
22 Mean precipitable water vapor (g/cm^2) derived from Nimbus 6 Scanning Microwave Spectrometer (SCAMS) for the period August 18, September 4, 1975. (after Grody, et al. 1978.)	43

FIGURES (Continued)

<u>Figure</u>	<u>Page</u>
23 Distribution of the index $(\bar{w} - w)/\bar{w} \times 10$, over the global oceans derived from the Nimbus 4 IRIS data for the period April, May and June, 1970. Positive value of this index gives a measure of the temperature increase from bottom to top of trade wind inversion in °C. Negative values of the index are shown by shading	44
24 Same as Fig. 23 but for the period July, August and September, 1970	45
25 Same as Fig. 23 but for the period October, November and December, 1970	46

PRECEDING PAGE BLANK NOT FILMED

INFERENCE OF THE BOUNDARY LAYER STRUCTURE OVER THE OCEANS FROM SATELLITE INFRARED MEASUREMENTS

INTRODUCTION

Temperature profile in the atmosphere has been successfully derived from passive infrared and microwave radiation measurements made from remote platforms (see for ex. Wark and Fleming, 1966; Conrath et al., 1970; Staelin et al., 1975; Smith and Woolf, 1976). In the infrared, spectral measurements in the vibration rotation bands of CO_2 at 15 and $4.3 \mu\text{m}$ are used for this purpose, while in the microwave the measurements in oxygen, O_2 , bands around 55 GHz (0.5 cm) are used. Both these gases, CO_2 and O_2 , are uniformly mixed in the atmosphere and hence their concentration decreases, with height, with a scale height of about 8 km. As such the weighting function for different spectral regions in the absorption bands of CO_2 and O_2 tend to be broad. For this reason the vertical resolution of the remotely sensed temperature profile from CO_2 and O_2 bands is rather poor. In particular the vertical resolution of the temperature profile in the lower troposphere is about 5 km which results in smoothing out of some meteorologically important small scale temperature features.

Water vapor in the atmosphere has a much smaller scale height of about 2 km and is heavily concentrated in the lowest layers of the atmosphere. However, unlike CO_2 and O_2 , vertical distribution of water vapor in the atmosphere is highly variable, particularly over land, which makes it difficult to use water vapor as an optically active gas to do remote sensing of temperature. This difficulty is substantially removed on large water bodies where it is possible to model the mean relative humidity profile with the help of climatology.

This mean relative humidity profile is significantly modified in the intertropical convergence zone (ITCZ) and in the trade wind inversion regime. When a low level convergence is present in the atmosphere, a deep convective layer is formed and this layer tends to have a high relative humidity. On the other hand if stable conditions in the temperature profile,

such as an inversion, exist, the water vapor is not convected up freely, and above the inversion usually a dry layer with low relative humidity exists. In this fashion strong correlation between the temperature and water vapor profiles is developed over water bodies depending on the conditions prevailing in the boundary layer. Given this a priori information of the correlation we can infer from the water vapor spectral measurements some details in the temperature profile close to the surface. In this study we have followed this approach to remotely sense the characteristics of the boundary layer of the atmosphere over the global oceans between about 50°N to 40°S for three different periods, about 3 months each, during the year 1970. The spectral measurements made by Nimbus 4 Infrared Interferometer Spectrometer (IRIS) are used for this purpose.

EXAMINATION OF THE INFORMATION CONTENT IN IRIS SPECTRA

The Nimbus 4 IRIS gathered spectral measurements from 400 cm^{-1} to about 1400 cm^{-1} over the globe for a period of about one year (April 1970 to Jan. 1971). The spectral resolution of this instrument is 2.8 cm^{-1} and the noise in the spectral data is about $0.5\text{ erg cm}^{-1}\text{ sr}^{-1}\text{ s}^{-1}$ (Hanel et al., 1972). The field of view of the IRIS is about 95 km in diameter. In Fig. 1 a typical brightness temperature spectrum of IRIS is shown. The $15\text{ }\mu\text{m}$ CO_2 band and $9.6\text{ }\mu\text{m}$ O_3 band are distinctly shown in the spectrum. The various water vapor bands, the rotation band around $20\text{ }\mu\text{m}$, the window regions at $11\text{ }\mu\text{m}$ and $9\text{ }\mu\text{m}$, and the $6.3\text{ }\mu\text{m}$ vibration rotation band, show some spectral details at 2.8 cm^{-1} resolution. These spectral details are produced by the water vapor lines which are distributed in some random fashion. Whenever a few strong water vapor lines come close together a strong minimum in the brightness temperature can be noticed. This implies that even at 2.8 cm^{-1} resolution we have some crude information of the water vapor lines retained in the spectral data. On the other hand the line information in the CO_2 and ozone bands is almost completely smeared out at 2.8 cm^{-1} resolution as the spectral lines in these bands are more closely arranged compared to the water vapor bands.

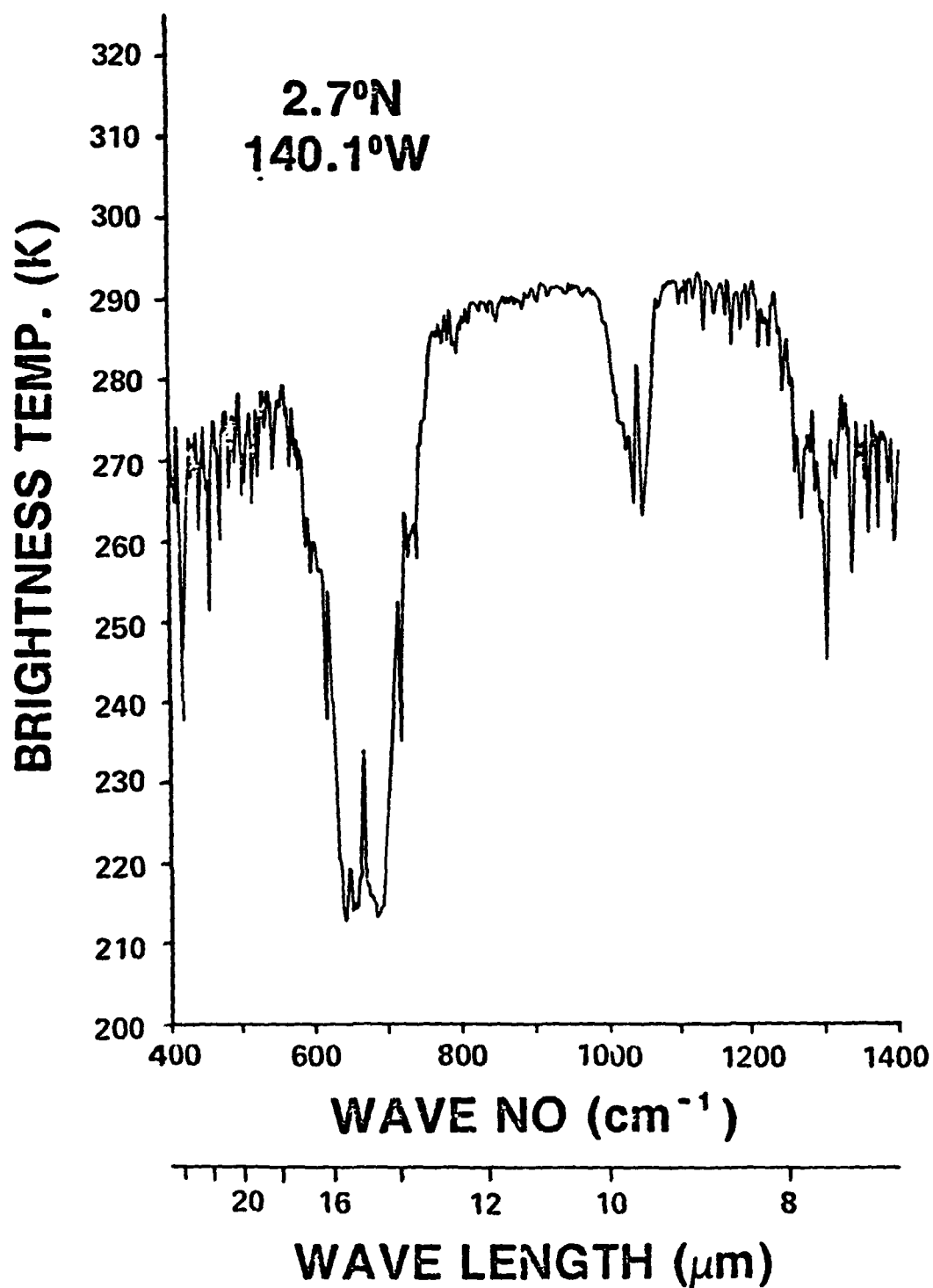


Figure 1. Nimbus 4 IRIS brightness temperature spectrum taken over the equatorial Pacific (2.7°N, 140.1°W, April 20, 1970). Notice the crude structure of the water vapor lines at 2.8 cm⁻¹ resolution in the 9 μm region (1100 - 1230 cm⁻¹)

The sharp maxima (peaks) and minima (valleys) in the water vapor bands suggest that the absorption coefficient of water vapor changes significantly in narrow spectral intervals. This implies further that radiances, corresponding to the brightness temperature, at the peaks and valleys in the spectrum, arise from significantly different altitudes in the atmosphere.

In this study we are interested in examining the information pertaining to the lowest layers in the atmosphere. Hence we have considered the water vapor spectral information in the window regions of 11–13 μm and 8–9 μm . These window regions are referred to as 11 μm and 9 μm regions respectively. In the 9 μm region the continuum absorption due to self-broadening effect is weaker (Bignell, 1970; Burch, 1970) while the lines are stronger as compared to the 11 μm region. For this reason we have considered the 9 μm region for the purpose of the present study. In order to appreciate the nature of the water vapor lines in the 9 μm region we have shown in Fig. 2a the transmission function of the water vapor, for 2 gms of precipitable water in the atmosphere, produced by a detailed line by line calculation at resolution of 0.1 cm^{-1} (Kunde and Maguire, 1974). Fig. 2b shows the transmission function when degraded to a resolution of 2.8 cm^{-1} , revealing that the water vapor line information is not obliterated at this resolution.

From an examination of Fig. 2b and the 9 μm window region shown in Fig. 1, we infer that in the peaks, produced by weak continuum absorptions; information close to the surface is being sensed. This corresponds, to a close approximation, to the surface temperature. The valleys on the other hand, formed by moderately strong lines, sense an effective temperature some what higher up in the atmosphere. The difference between the peaks and valleys, which ranges from about 1 to 12°C in temperature, as will be shown later, gives us some information about the structure of the atmosphere in the first 2 or 3 km near the surface.

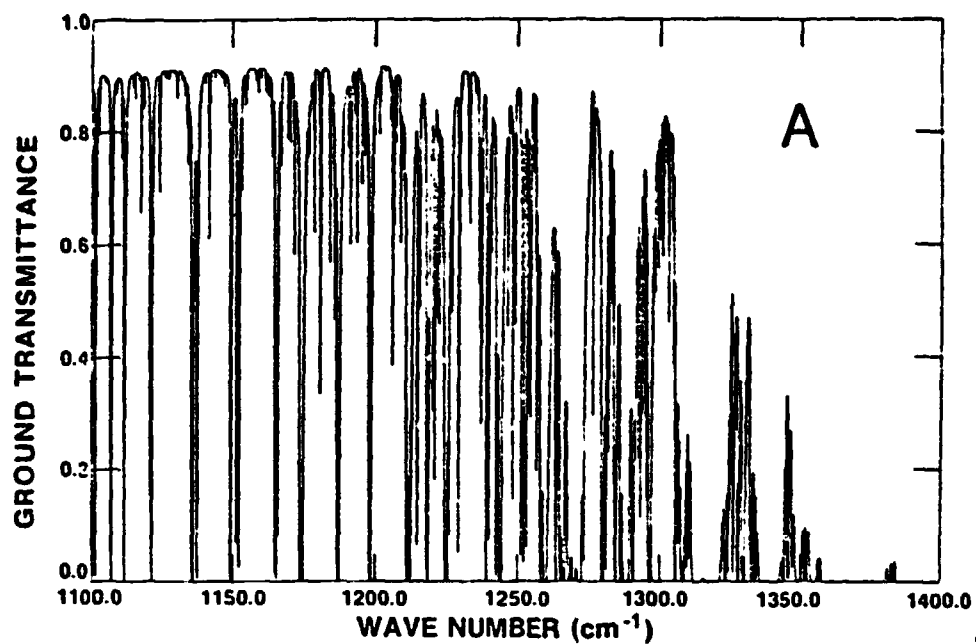


Figure 2a. Water vapor transmission function at 0.1 cm⁻¹ resolution (Kunde and Maguire, 1974) for 2 g/cm² of precipitable water.

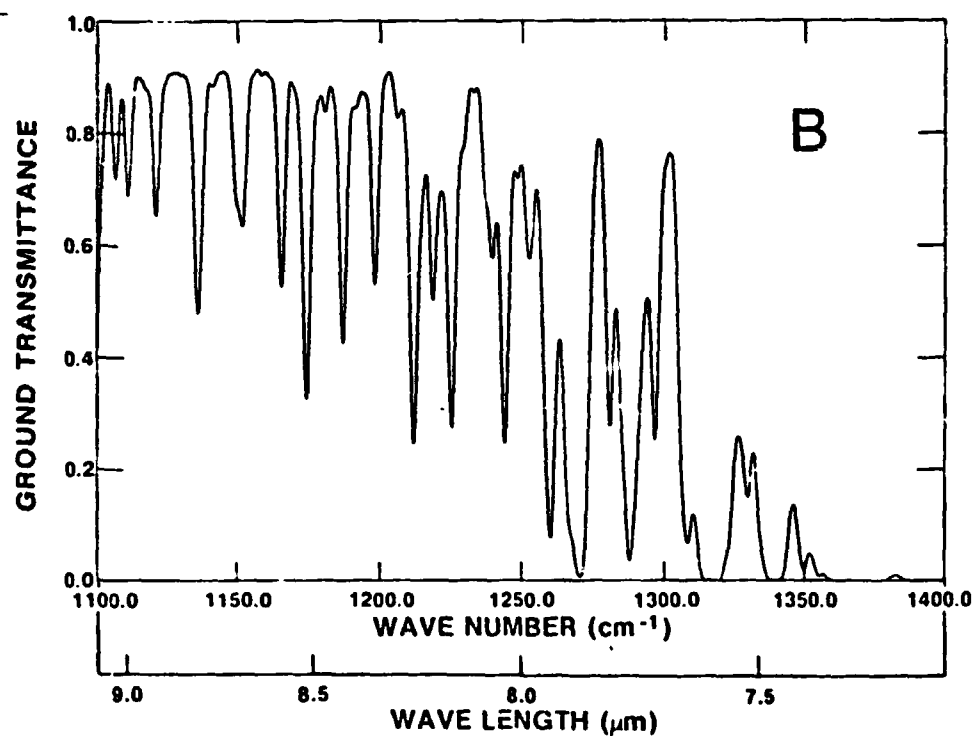


Figure 2b. Same as Fig. 2a when degraded to 2.8 cm⁻¹ resolution.

THEORETICAL CONSIDERATIONS

It was pointed out in the previous section that the water vapor spectral measurements in the $9\text{ }\mu\text{m}$ window region could yield information about the atmospheric stratification in the boundary layer over the oceans. We will develop this idea using the radiative transfer theory.

The intensity I_ν measured at the top of the atmosphere, at wave number ν , in a non-scattering atmosphere in local thermodynamic equilibrium, is given by

$$I_\nu = B_\nu(p_0) \tau_\nu(p_0) + \int_{\tau_\nu(p_0)}^1 B_\nu(p) d\tau_\nu(p) \quad (1)$$

where

B is the Planck intensity,

$\tau(p)$ is the transmission of the atmosphere from any given pressure p to the top of the atmosphere,

p_0 is the surface pressure.

When we apply this equation to the spectral data in the $9\text{ }\mu\text{m}$ water vapor window region, the first term on the right hand side, i.e. the contribution from surface is essentially governed by the surface temperature and the total precipitable water content in the atmosphere. The second term accounts for the emission of the whole atmosphere, and it depends on the manner in which the water vapor and temperature are distributed. Within the $9\text{ }\mu\text{m}$ window, as shown in the IRIS spectrum (Fig. 1), at the peaks where the absorption is weak the contribution from the second term is much smaller than the first one. Thus the intensity at these peaks depends only weakly on the atmospheric stratification. However, in the valleys of the spectrum, where the absorption is considerably larger, the second term in the equation exceeds the first one. Now if we take the difference ΔI between the intensity at the peak, I_p , and the intensity I_v in the valley, we get some information about the atmospheric structure.

An equation for ΔI may be derived from equation (1) as follows

$$\Delta I = I_p - I_v \cong \tilde{B}(p_0) [\tau_p(p_0) - \tau_v(p_0)] + \int_{[\tau_p(p_0) - \tau_v(p_0)]}^0 \tilde{B}(p) d [\tau_p(p) - \tau_v(p)] \quad (2)$$

where \tilde{B} is the average Planck intensity corresponding to the peak and valley in the spectrum which are spaced within 10 cm^{-1}

and τ_p and τ_v are the transmissions in the peak and valley of the spectrum.

From equation (2) we see that ΔI will be zero when the atmosphere is isothermal having a temperature equal to the surface temperature. On the other hand if the temperature increases from the surface to considerable height ΔI can be negative. Such negative values are commonly noticed in the polar latitudes.

Equation (2) may be generalized as

$$\ell = f [T_s, T(p), R.H.(p)] \quad (3)$$

where the line strength ℓ is the brightness temperature difference corresponding to ΔI , $T(p)$ and $R.H.(p)$ are the temperature and relative humidity distributions as a function of pressure, p , in the atmosphere,

T_s is the surface temperature.

Now if we are given the mean conditions of temperature profile, $\bar{T}(p)$, associated with a given surface temperature T_s and relative humidity profile, $\bar{R.H.}(p)$, we can express the line strength $\bar{\ell}$ corresponding to these mean condition as

$$\bar{\ell} = f [T_s, \bar{T}(p), \bar{R.H.}(p)] \quad (4)$$

When the temperature and the relative humidity profiles in the atmosphere for a given T_s differ from such mean conditions the line strength ℓ departs from $\bar{\ell}$ by an amount, say $\Delta \ell$.

Such a perturbation $\Delta\ell$ can then be expressed as

$$\Delta\ell = \bar{\ell} - \ell = g [T_s, T'(p), R.H.'(p)] \quad (5)$$

where T' and $R.H.'$ are deviations from average.

The surface temperature T_s can be determined independently from the $11\ \mu\text{m}$ window measurements of IRIS using a method developed by Prabhakara et al., (1974). Thus from equation (5) we see that from one quantity, $\Delta\ell$, we can infer one dominant mode or property of the atmosphere implicitly contained in the right hand side of the equation. On the water bodies, as will be discussed later, the intimate relationship between the characteristics of the temperature and water vapor profile in the boundary layer can be modelled to define such a dominant mode.

SPECTRAL SIMULATIONS FOR DIFFERENT ATMOSPHERIC MODELS

In order to study the manner in which ℓ , as defined previously, changes as a function of the atmospheric conditions we have developed a radiation computational scheme that can simulate the spectral data with a resolution of $2.8\ \text{cm}^{-1}$ in the water vapor absorption regions from $400\ \text{cm}^{-1}$ to $1400\ \text{cm}^{-1}$. The transmission function, τ , of the water vapor needed in these calculations is taken to be the product of three components: τ_l associated with water vapor lines, τ_p produced by the continuum due to foreign broadening, and τ_e resulting from the e-type absorption (Bignell, 1970). The transmission function of the water vapor lines τ_l is derived using a multiple regression scheme similar to the one proposed by Smith (1969). The details of the foreign broadening and the e-type given by Kurde and Maguire (1974) are adopted.

This simulation program is used to synthesize spectral data for several different atmospheres ranging from tropics to high latitudes. The atmospheric temperature and relative humidity distributions corresponding to mean conditions in the latitudinal belts 0 to 10° , 10 to 30° ,

and 30° to 50° on both the hemispheres for four seasons are derived by Nieman (1977), from radiosonde data measured during the year 1972, over the globe (see Table 1). Some of these mean profiles of the temperature and relative humidity are shown in Fig. 3. It is interesting to note that in all cases the mean relative humidity profile is very similar and decreases from surface up to about 200 mb almost linearly as a function of height. These data are heavily weighted by land stations. However, from a limited sample of ship and island radiosonde data taken over north Atlantic (see Tables 6a and 6b) during the year 1970, we find a mean value of 81% relative humidity near the surface, and a similar decrease with height. For this reason we have adopted for the radiative transfer simulations, one relative humidity profile, as shown in Fig. 3, for all oceanic regions.

From the synthetic spectral data, calculated with the simulation program, using the above mean atmospheric conditions, we have obtained the brightness temperature at eight peaks in the $9\ \mu\text{m}$ region - 1127.7, 1140.2, 1158.3, 1168.0, 1181.9, 1193.1, 1202.8, 1232.0 cm^{-1} - and averaged them. Similarly the brightness temperature at eight adjacent valleys - 1136.1, 1149.9, 1165.3, 1173.6, 1186.1, 1197.2, 1211.2, 1225.1 cm^{-1} - are averaged. The difference between these two averages gives an estimate of the line strength representative of the spectral region 1125 to 1235 cm^{-1} . This value of $\bar{\ell}$, in brightness temperature, is shown in Table 2 for the various mean atmospheres. In Fig. 4 we show graphically the relationship between the surface temperature of the various model atmospheres and $\bar{\ell}$. The total precipitable water content \bar{w} is also shown in this figure as a function of the surface temperature. Both \bar{w} and $\bar{\ell}$, as seen from the figure 4, increase with T_s in an analogous fashion. The increase in \bar{w} may be readily understood in terms of the moisture holding capacity of the warmer atmospheres. The growth of $\bar{\ell}$ needs some explanation.

The behavior of $\bar{\ell}$ can be explained with the help of the weighting functions, $d\tau/dz$, associated with the valleys and peaks in the spectra. In Fig. 5 the weighting function corresponding

Table 1

Mean profiles of relative humidity and temperature for different latitude belts and seasons (From Nieman, 1977).

Latitude Belt	Tropics		Subtrop. Summer		Subtrop. Winter		Temperate Summer		Temperate Winter	
	10°N – 10°S		10°N – 30°N		10°N – 30°N		30°N – 50°N		30°N – 50°N	
Pressure (mb)	T(K)	R.H(%)	T(K)	R.H(%)	T(K)	R.H(%)	T(K)	R.H(%)	T(K)	R.H(%)
1000	298.9	79.4	298.6	78.0	291.9	74.4	292.8	69.9	273.9	71.5
920	294.2	76.9	294.9	74.8	287.8	72.5	290.9	61.7	271.1	71.0
850	290.2	72.7	291.4	68.4	284.9	65.5	288.3	57.0	268.9	64.3
700	282.3	55.7	282.8	52.8	278.4	45.3	278.7	51.3	263.3	50.6
600	275.2	50.6	275.4	50.6	271.9	38.9	271.0	47.4	257.0	47.4
500	267.4	41.9	267.1	44.2	263.5	28.1	262.0	41.8	248.5	41.9
400	256.8	33.7	256.4	36.9	252.1	25.8	250.5	36.3	237.5	25.6
300	241.6	28.0	241.8	29.7	237.6	13.5	235.5	16.8	224.4	1.4
200	219.7	1.5	220.4	1.4	219.2	0.4	220.3	0.7	216.1	0.1
100	194.8	0.1	200.0	0.1	198.8	0.1	212.6	0.1	213.7	0.0

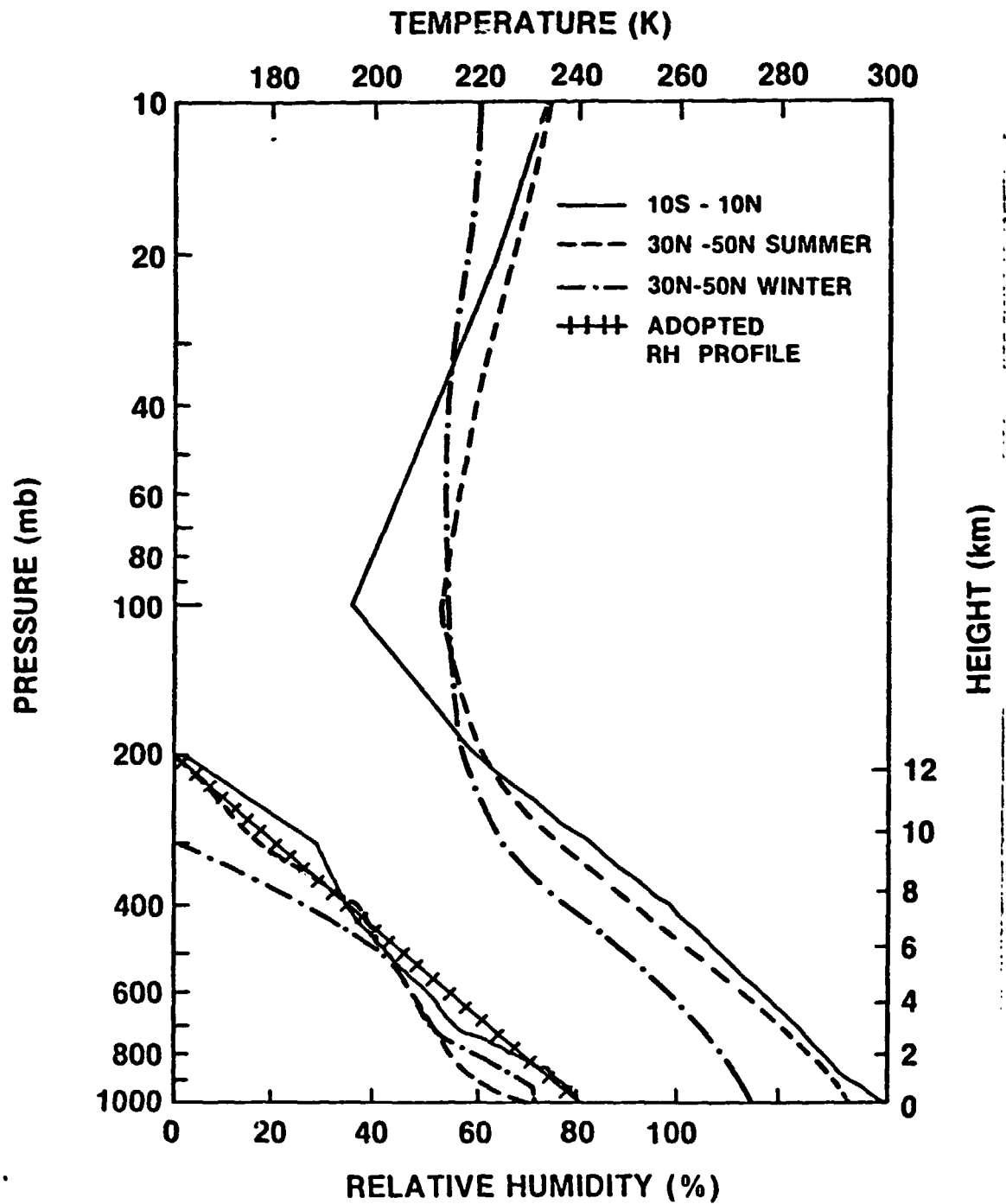


Figure 3. Mean relative humidity and temperature profiles for tropics and midlatitudes summer and winter (from Nieman, 1977). The adopted R.H. profile is also shown.

Table 2

Mean line strength $\bar{\ell}$ and total precipitable water \bar{w} as a function of the surface temperature T_s for different mean atmospheres.

	$T_s(K)$	$\bar{\ell} (^{\circ}C)$	$\bar{w} (g/cm^2)$
Tropics 10°N - 10°S	298.9	9.4	4.28
Subtropics Summer 10°N - 30°N	298.6	9.3	4.29
Subtropics Winter 10°N - 30°N	291.9	6.6	2.67
Temperate Summer 30°N - 50°N	292.8	7.1	2.91
Temperate Winter 30°N - 50°N	273.9	2.8	0.92

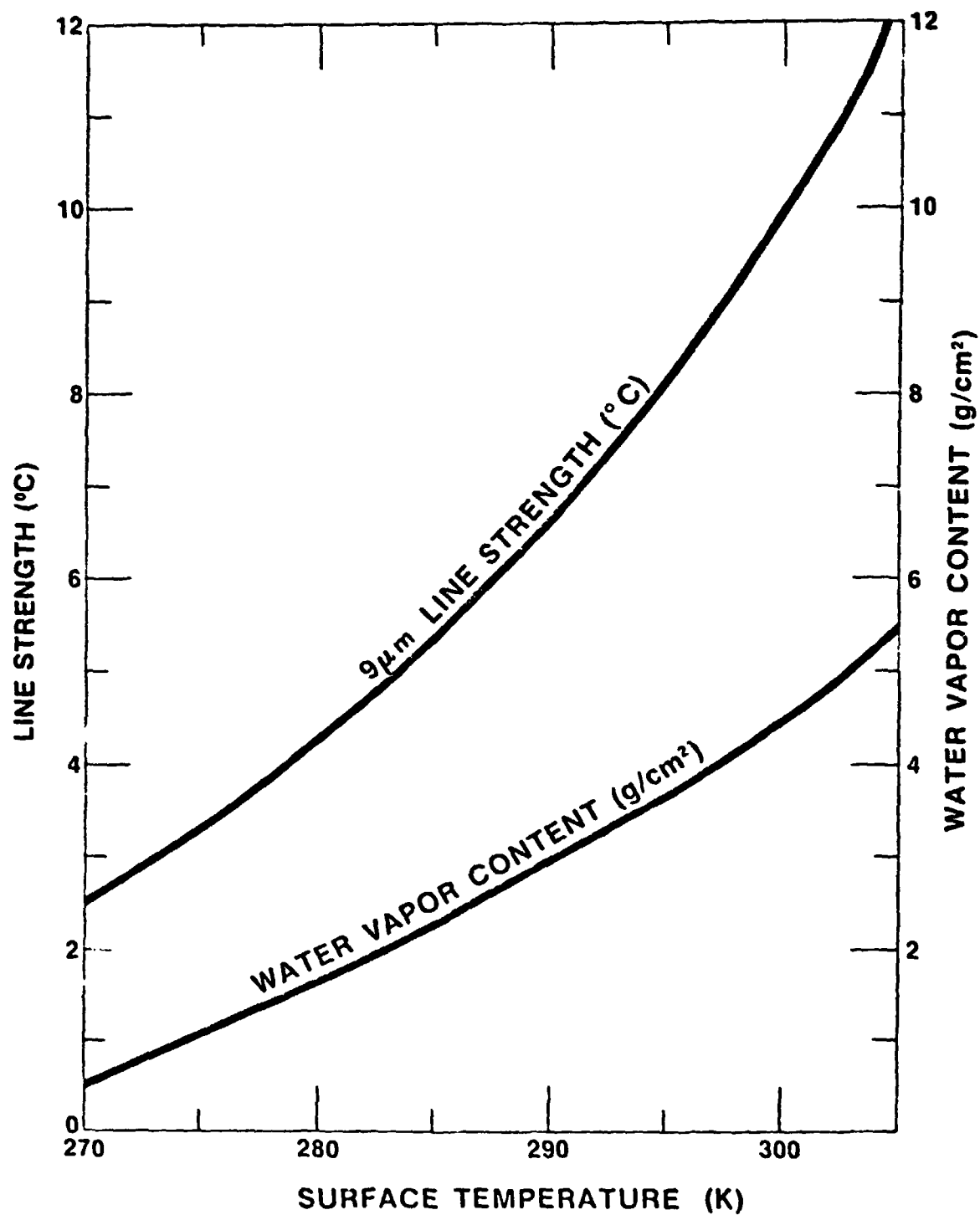


Figure 4. Dependence of the $9\mu\text{m}$ mean line strength $\bar{\epsilon}$ and the total water vapor content \bar{w} on the surface temperature T_s over the oceans.

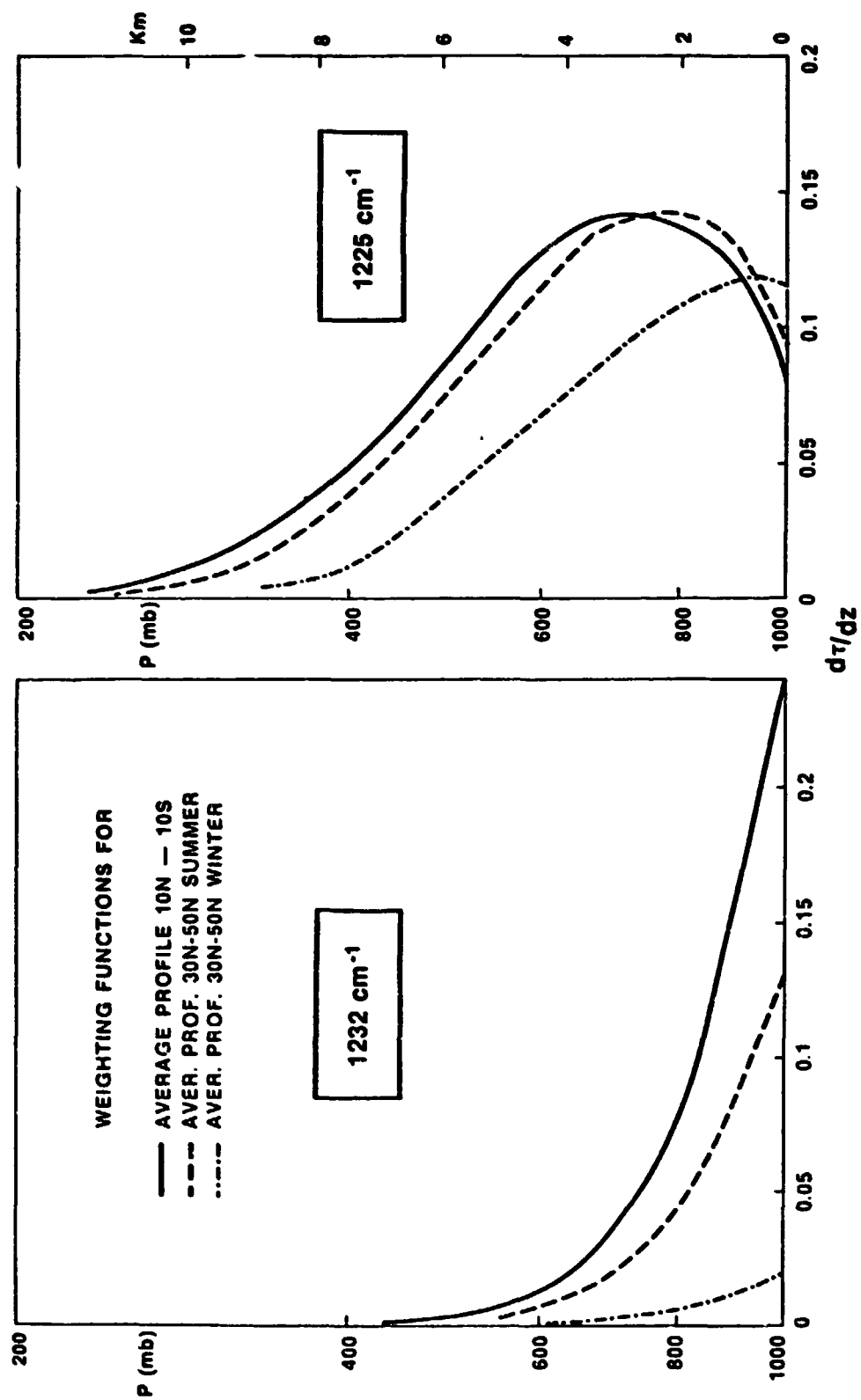


Figure 5. Weighting functions for the peak at 1232 cm⁻¹ and valley at 1225 cm⁻¹ for the three mean atmospheric conditions.

to a valley at 1225 cm^{-1} and adjacent peak at 1232 cm^{-1} are shown for three atmospheres. The weighting function associated with the valley has a distinct maximum which moves down from about 3 km to 1.5 km as the total water content decreases. The weighting function at the peak on the other hand does not show such a feature.

The height at which the maximum in the weighting function occurs is around unit optical depth in the atmosphere. At 1225 cm^{-1} , a valley in the spectrum, unit optical depth is reached at a higher elevation in a warmer and, therefore from climatology, more humid atmosphere. In the peak at 1232 cm^{-1} unit optical depth is not reached in all the cases.

The strength of the line ℓ is thus crucially dependent on the super incumbent water vapor in the troposphere. This relationship between ℓ and w is shown in Fig. 6 by a solid line. This pseudo linear relationship suggests that when mean conditions of temperature and humidity profiles are present ℓ grows in proportion to w .

From the above discussion we may conclude that, over the oceans, the relationships shown in Figs. 4 and 6 represent basic correlations among the surface temperature T_s , w and ℓ . These correlations may be broken when atmospheric temperature and water vapor profiles are perturbed from mean conditions. Such perturbations are present over the global oceans.

In the following discussion these climatologically significant perturbations are examined in some detail.

Trade wind inversion

Trade wind inversion is a climatological feature associated with oceanic subtropical anticyclones. In the northern hemisphere the axis of these anticyclones is tilting from NE to SW (see for ex. Haurwitz and Austin, 1942) and thereby the vertical motion associated with these anticyclones has an organized pattern. On the NE side there is a pronounced subsidence while on the SW the vertical motion is weak. This organized motion of the subtropical anticyclones produces strong inversion on the NE side. The observations of the Meteor oceanographic

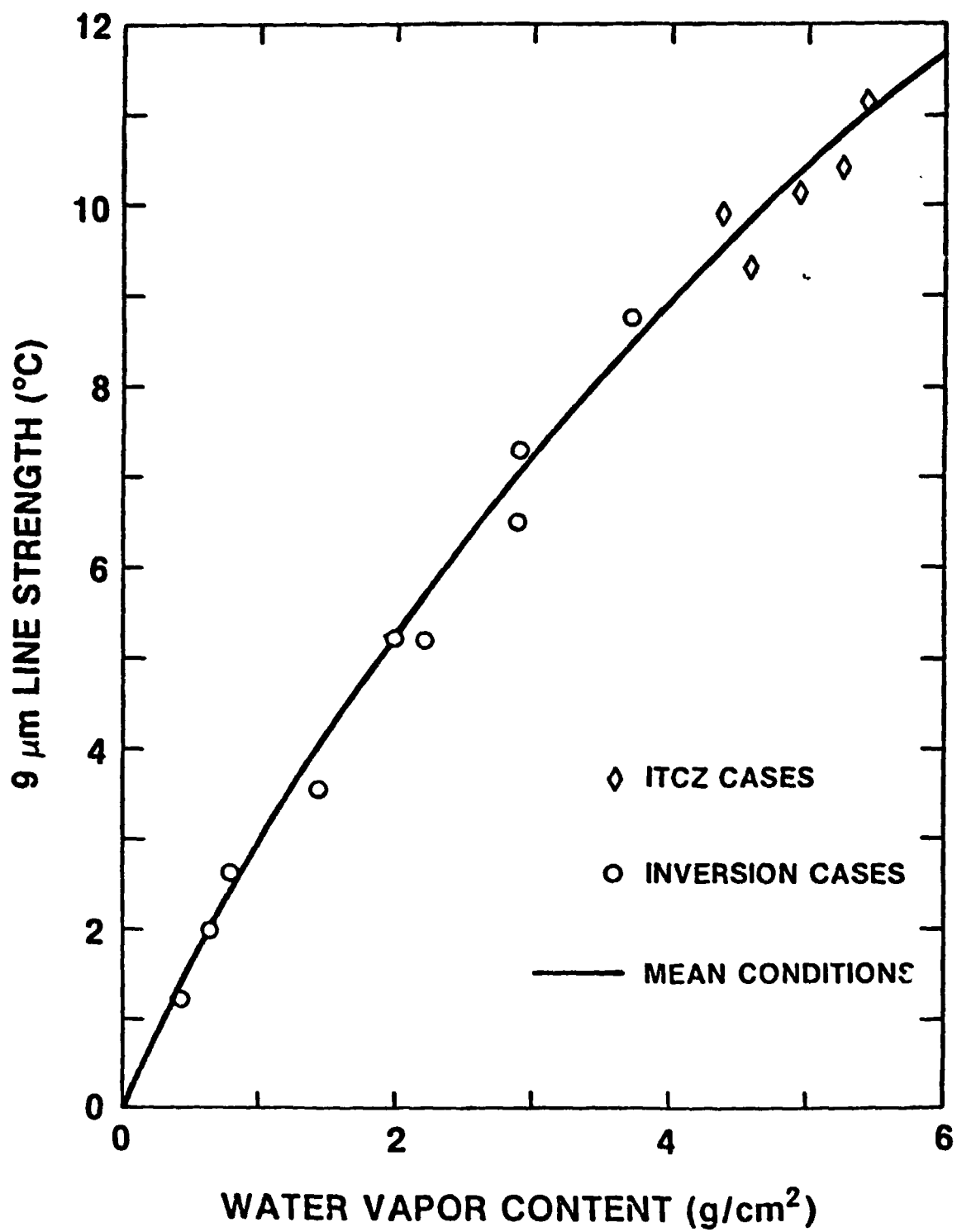


Figure 6. The relationship between the 9 μm line strength and the total precipitable water for mean atmospheric conditions, for inversion conditions (from Tables 4a, b and c), and ITCZ cases (see Tables 5a and b).

expedition (Ficker, 1936; Riehl, 1954) reveal the general nature of the trade wind inversion over the North and South Atlantic. The more recent experiments related to GATE, in particular BOMEX and ATEX (Augstein et al., 1973; Dunckel et al., 1974), reinforce the observations of the Meteor expedition.

In Fig. 7 an example of trade wind inversion is presented to illustrate the height of the inversion, the temperature increase ΔT from bottom to top of inversion and the corresponding decrease in relative humidity $\Delta R.H.$ Ficker (1936) has constructed, from Meteor data, maps of the change in temperature and relative humidity from bottom to top of the inversion, as well as a map of the height of the inversion. Riehl (1954) shows these maps and presents a lucid discussion. A close examination of these maps reveals intimate connection between the height of the inversion, the temperature change, and relative humidity change associated with the inversion. In Fig. 8 we show the manner in which the increase in temperature, ΔT , and the decrease in the relative humidity, $\Delta R.H.$, across the inversion, are related. This shows a good positive correlation between the two variables. In Fig. 9 the ΔT and the height of the inversion are related. This relationship is not as well defined as the previous one although a negative correlation between the two variables is suggested. These correlations are developed in a consistent fashion by subsidence motion. That is to say the stronger the subsidence the lower the height of the inversion and the larger the temperature increase from bottom to top due to adiabatic warming (Riehl, 1954). The change in relative humidity is primarily due to the capping of convection by the inversion, which limits the height of the lower humid layer, while above the inversion sinking of dry air and dynamic warming lower the relative humidity. In this manner a correlation between the temperature profile and the water vapor profile in the troposphere is developed on oceanic regions where the inversion conditions prevail.

The Indian Ocean expedition has revealed the inversion characteristics over the Arabian sea. From the measurements made along $50^{\circ}E$ by the ship R.V. Discovery, Ramage (1971)

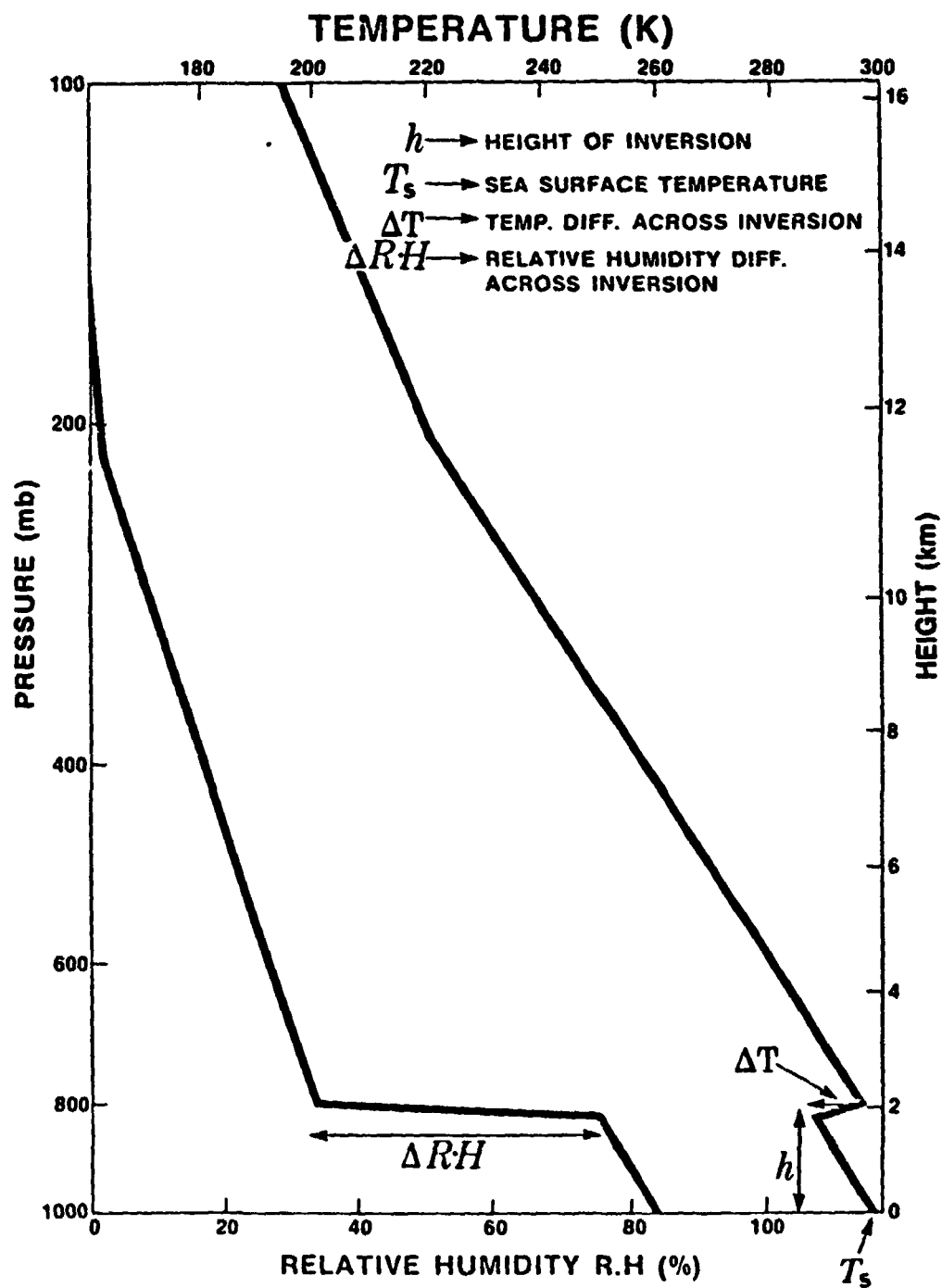


Figure 7. Example of temperature and relative humidity profiles in the trade wind inversion regime.

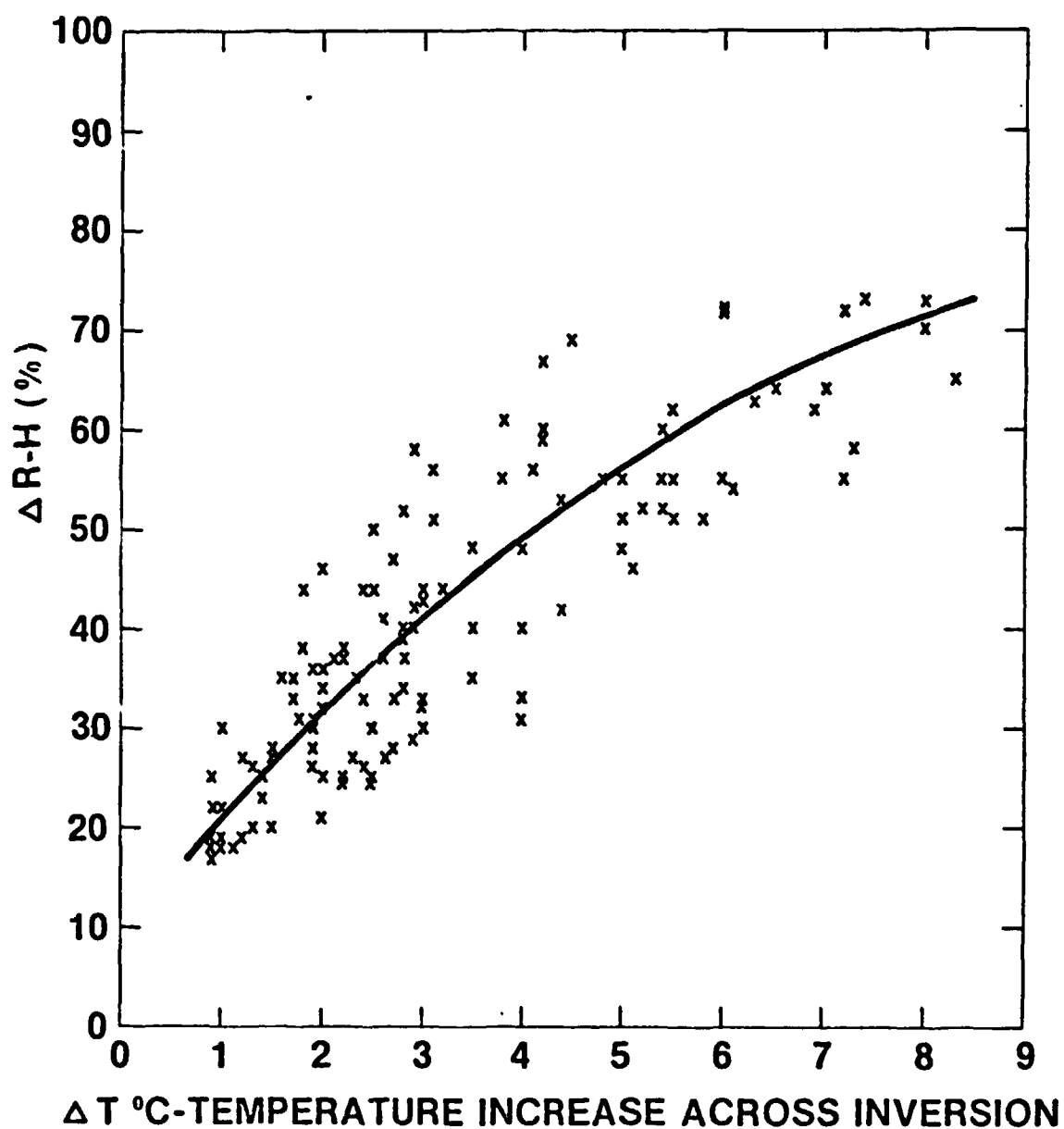


Figure 8. Relationship between the temperature increase, ΔT , and the decrease in relative humidity $\Delta R.H$ from bottom to top of inversion, derived from the observation of the Meteor expedition (Ficker, 1936).

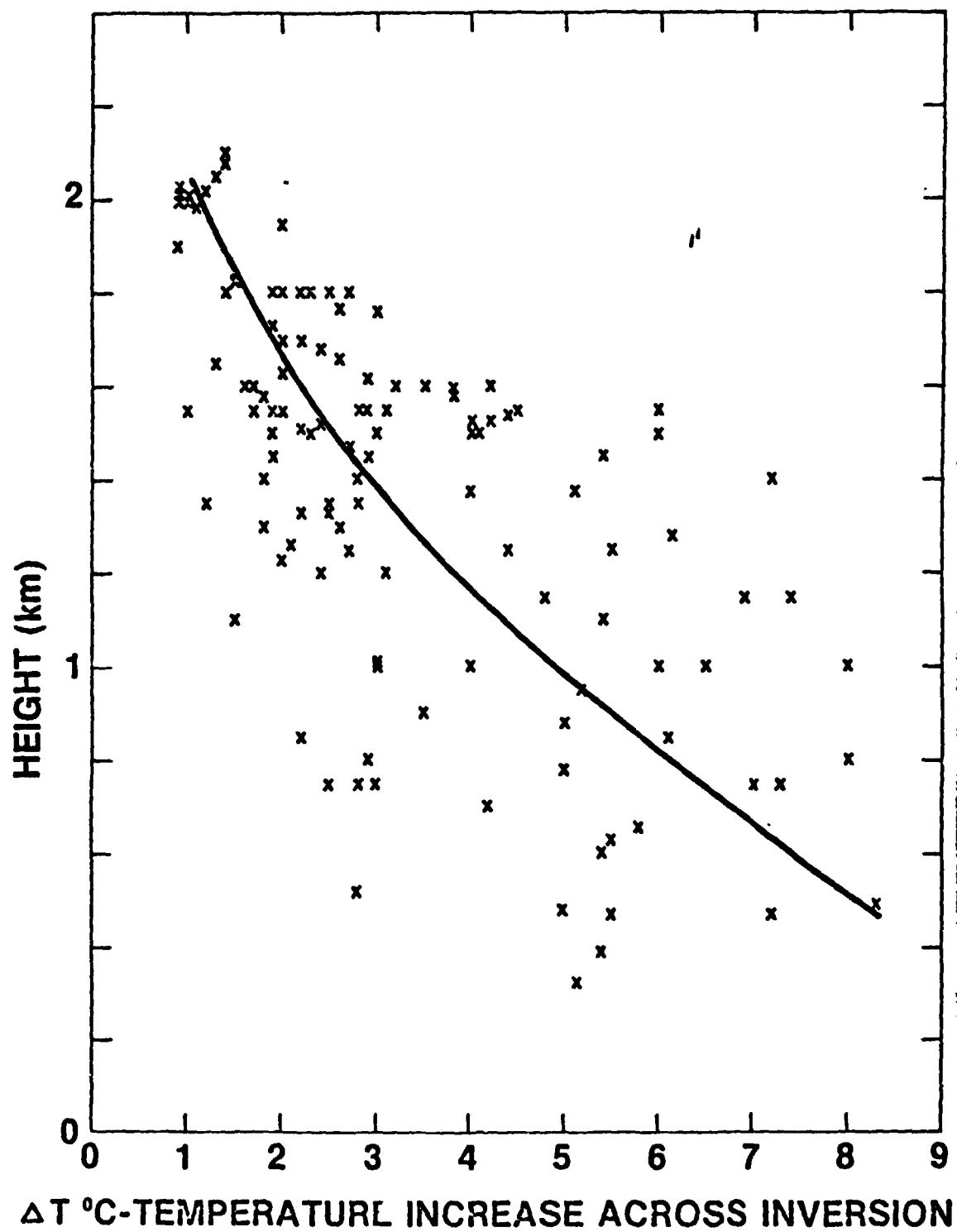


Figure 9. Relationship between the height h of the inversion and the increase in temperature from bottom to top of inversion derived from the observations of the Meteor expedition (Ficker, 1936).

shows a meridional cross section of the temperature and relative humidity distribution from 7°N to 12°N during August 1964. This cross section shows a significant temperature inversion, up to as much as 10°C warming at 10°N, between the surface and 1 km level. In another figure Ramage (1966) shows, from ship observations made during summers of 1963 and 1964, the distribution of the level of inversion over the Arabian sea and the adjoining Indian Ocean. The salient features of this distribution are that the height of the inversion is generally low, at about 1 km, close to the coast line of Somali, Arabia, Iran and Pakistan. Away from this coast line the height of the inversion rises to about 3 km as one goes toward Indian Ocean. In a broad sense the observations of the Indian Ocean Expedition reinforce those derived from the Meteor Expedition.

The graphical relationships shown in Figs. 8 and 9 enable us to model the inversion characteristics over the oceans with one parameter say ΔT which is coupled to $\Delta R.H$ and h . In Table 3, three values of the inversion parameter ΔT and the associated $\Delta R.H$ and h , derived from Figs. 8 and 9 are shown. These inversion characteristics are applied to the various mean atmospheres shown in Table 1. The temperature profile above the inversion layer is obtained by a straight line fit between the temperature at 500 mb and the temperature at the top of

Table 3

Three parameter representation (Fig. 7) of the trade wind inversion based on Meteor data (see Figs. 8 and 9).

Height of Inversion	Temp. Increase	Decrease in Rel. Hum.
h (km)	ΔT (°C)	$\Delta R.H$ (%)
1.70 (825 mb)	2	32
1.15 (880 mb)	4	48
0.75 (930 mb)	6	62

the inversion. The adopted relative humidity profile shown in Fig. 3 is suitably modified to represent the inversion conditions. Above the level of inversion the relative humidity profile is extrapolated assuming a constant value till it meets the undisturbed profile. In Fig. 10 these three relative humidity profiles of the trade wind inversion are shown. Applying these three inversion characteristics to the tropical, mid latitude summer and the mid latitude winter atmospheres (see Table 1) we have calculated ℓ , the strength of the lines in the $9\ \mu\text{m}$ region. In Tables 4a, b and c, the strength of ℓ and the total precipitable water w for the three inversion conditions are listed. These tables show the dependence of ℓ on the boundary layer parameters h , ΔT and $\Delta R.H$ in a joint fashion. We have attempted to decouple the dependence on these parameters and examine the sensitivity of ℓ separately to the temperature profile, the water vapor profile and the height of the inversion level. Such an examination shows that about 85% of the change in ℓ is due to the variation in the water vapor profile, while the temperature profile accounts for about 10% and h accounts for about 5%. The above analysis shows the overwhelming importance of the water vapor profile. Any inference of the temperature profile from ℓ thus has to be deduced by way of statistical correlation with respect to water vapor profile.

For a given surface temperature the total water content in each one of these models varies as the boundary layer parameters change. The water content is at a maximum when the inversion is absent and least when the inversion is at the lowest levels as shown in the Tables. As the total water is an integral property reflecting the inversion characteristic we may relate it to ℓ .

In Fig. 6 the values of ℓ and w taken from Tables 4a, b, c, are plotted. It can be seen from this figure that all the points are very close to the curve corresponding to mean atmospheric conditions. As a consequence of this result it is possible to infer w from ℓ in the presence of the inversion condition.

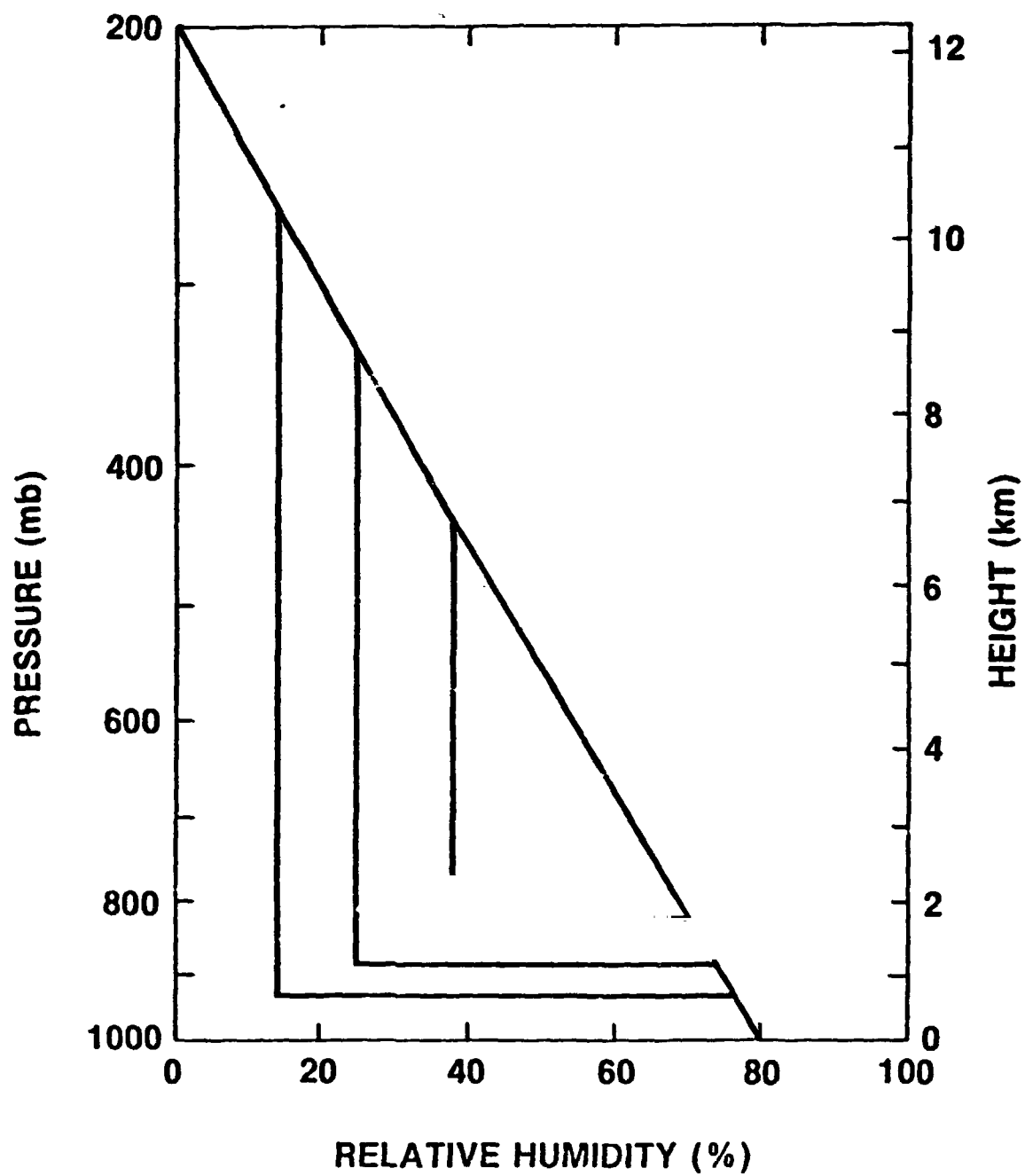


Figure 10. Adopted mean relative humidity profile (shown also in Fig. 3) and the models of the relative humidity profile for three conditions (see Table 3) of the inversion.

Table 4

Computed $9\ \mu\text{m}$ line strength corresponding to three trade wind inversions (see Table 3) for tropics (a), mid-latitude summer (b) and mid-latitude winter (c).

(a) Tropical mean atmosphere ($T_s = 298.9\ \text{K}$, $\bar{\ell} = 9.62^\circ\text{C}$, $\bar{w} = 4.28\ \text{g/cm}^2$)

h (km)	$\Delta T\ (^{\circ}\text{C})$	$\Delta\text{R.H. (\%)}$	$\ell\ (^{\circ}\text{C})$	w (g/cm ²)	$(\bar{w} - w)/\bar{w}$
1.70	2	32	8.75	3.71	0.13
1.15	4	48	7.30	2.91	0.32
0.75	6	62	5.22	1.98	0.54

(b) Midlatitude Summer ($T_s = 292.6\ \text{K}$, $\bar{\ell} = 7.48^\circ\text{C}$, $\bar{w} = 3.35\ \text{g/cm}^2$)

h (km)	$\Delta T\ (^{\circ}\text{C})$	$\Delta\text{R.H. (\%)}$	$\ell\ (^{\circ}\text{C})$	w (g/cm ²)	$(\bar{w} - w)/\bar{w}$
1.70	2	32	6.51	2.89	0.14
1.15	4	48	5.18	2.22	0.34
0.75	6	62	3.54	1.46	0.56

(c) Midlatitude Winter ($T_s = 273.8\ \text{K}$, $\bar{\ell} = 3.10^\circ\text{C}$, $\bar{w} = 0.96\ \text{g/cm}^2$)

h (km)	$\Delta T\ (^{\circ}\text{C})$	$\Delta\text{R.H. (\%)}$	$\ell\ (^{\circ}\text{C})$	w (g/cm ²)	$(\bar{w} - w)/\bar{w}$
1.70	2	32	2.62	0.81	0.16
1.15	4	48	1.97	0.65	0.35
0.75	6	62	1.22	0.43	0.57

The surface temperature T_s on the ocean can be measured independently from the $11\ \mu\text{m}$ IRIS window data. Given the surface temperature we can estimate the total water content \bar{w} corresponding to mean atmospheric condition, from Fig. 4. Now if we can combine the parameters of the inversion in a model, as discussed earlier, we can relate $(\bar{w} - w)/\bar{w}$ to the strength of the inversion parameters. We find the relationship applicable to ΔT is

$$(\bar{w} - w)/\bar{w} = A \Delta T \quad (6)$$

where A is a constant approximately equal to 0.1°C^{-1} .

This relationship is shown in Fig. 11.

Inter Tropical Convergence Zone. ITCZ

Another well known phenomenon over the tropical oceans is the Inter Tropical Convergence Zone, ITCZ. This is the region where the low level winds converge to produce a rising motion which carries water vapor upward and produces above average humidity conditions aloft. The temperature inversion above the boundary layer in the ITCZ is generally absent or weak (Estoque, 1975). Thus the temperature profile in the ITCZ areas does not show a significant departure from mean atmospheric conditions. However the water vapor profile reflects the effects of rising motion, resulting in a significant increase in total water content. For this reason we can not develop a simple model of the coupling of the temperature and water vapor profiles in the ITCZ.

Observations of the temperature and humidity corresponding to the ITCZ conditions are given in the studies of Augstein et al. (1974), Estoque (1975), Godbole and Ghosh (1975), and Estoque and Douglas (1978). In Table 5a these data are shown. The relative humidity profile in the ITCZ shows a significantly larger value than the climatological average between about 800 and 600 mb. In this region of the atmosphere significant deficit in humidity is noticed when inversion conditions prevail. Utilizing the radiative transfer program we have calculated the $9\mu\text{m}$ line strength for all these ITCZ cases which are shown in Table 5b.

The values of ℓ and the corresponding w for the ITCZ case is also plotted in the Fig. 6. This Figure clearly shows that the ITCZ ℓ values conform reasonably well with the general ℓ vs. w relationship that was derived from mean atmospheric conditions and trade wind inversion models. In all the ITCZ cases the parameter $(\bar{w} - w)/\bar{w}$ is negative (see Table 5b) suggesting that the water vapor content and the depth of the humid layer exceed average conditions.

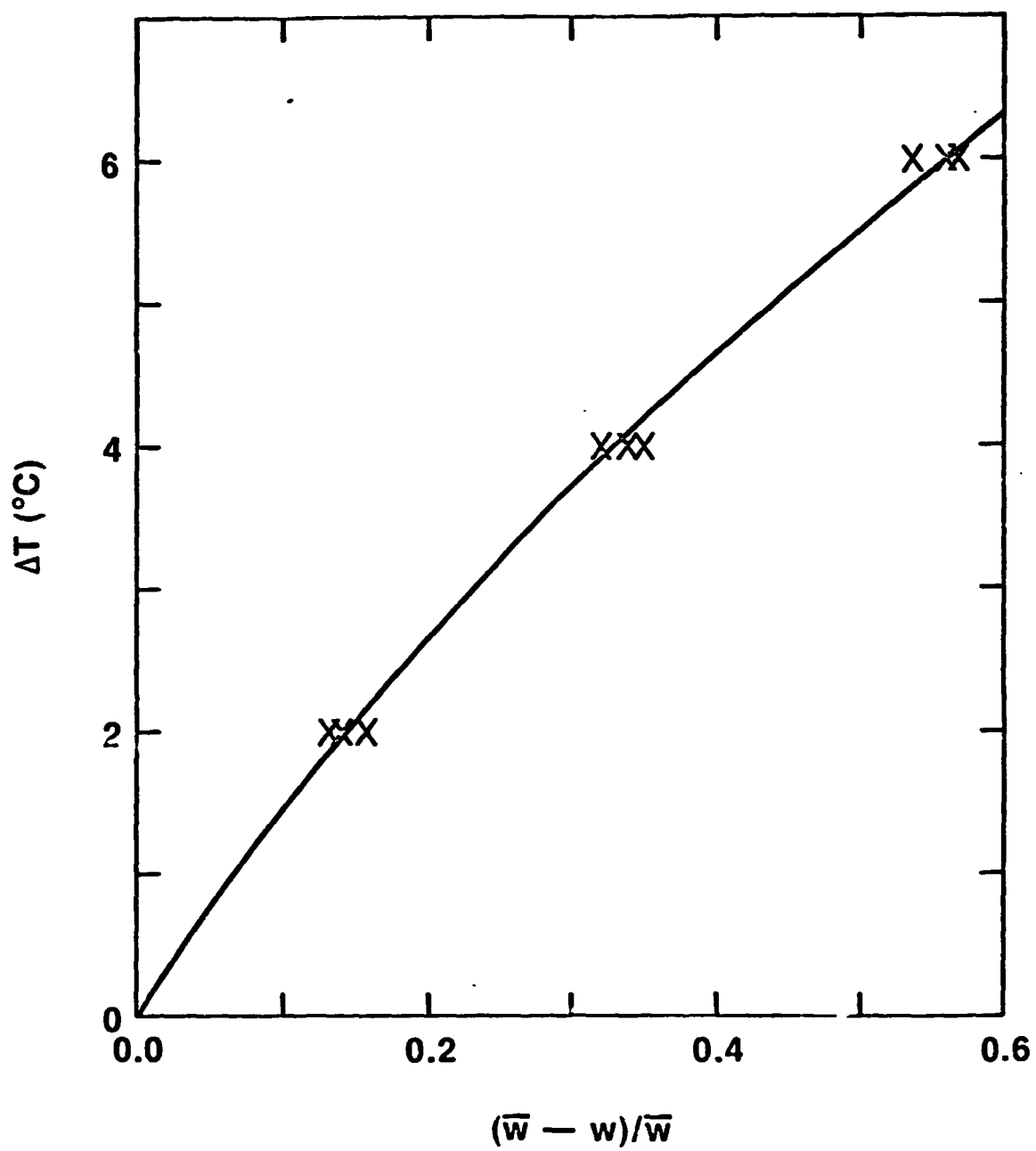


Figure 11. Relationship between the temperature increase ΔT , from bottom to top of the inversion and the index $(\bar{w} - w)/\bar{w}$ based on the data given in Table 4.

Table 5a

Temperature and relative humidity profiles for observed cases of ITCZ.

Pressure (mb)		1000	950	900	850	800	700	600	500	400	300	200	100
JORDAN (1958)	T (K)	299.2	296.2	293.0	290.5	287.8	281.8	274.6	266.3	255.5	240.0	218.0	199.7
	R.H (%)	84.3	83.3	81.6	76.3	65.2	58.6	51.5	46.4	33.8	32.3	28.3	0.0
AUGSTEIN (1974)	T (K)	299.2	296.2	293.2	291.2	288.8	283.8	277.2	266.3	255.8	240.0	218.0	199.7
	R.H (%)	86.2	76.3	86.8	79.6	72.8	61.8	72.3	53.0	41.7	25.9	28.3	0.0
ESTOQUE a (1975)	T (K)	297.7	295.0	292.0	289.5	287.0	281.7	274.8	266.9	256.1	240.0	218.0	199.7
	R.H (%)	89.6	92.6	94.9	91.7	82.5	82.4	76.2	69.6	56.2	32.3	28.3	0.0
ESTOQUE b (1978)	T (K)	298.7	295.2	291.7	289.2	286.8	284.8	276.6	267.3	257.5	242.0	219.0	199.7
	R.H (%)	79.5	82.8	86.5	67.8	100.0	47.9	44.6	43.0	25.6	26.7	25.1	0.0
GODBOLE (1975)	T (K)	299.7	296.2	292.8	288.8	286.2	278.7	272.7	266.7	256.1	240.0	218.0	199.7
	R.H (%)	87.1	90.8	94.2	100.0	99.4	98.1	93.0	75.0	37.7	27.7	23.0	15.0

Table 5b

Calculated $9\ \mu\text{m}$ line strength, the total water content w ,
and the index $(\bar{w} - w)/\bar{w}$ for the ITCZ cases.

	$T_s(\text{K})$	$\ell(^{\circ}\text{C})$	$w\ (\text{g}/\text{cm}^2)$	$\bar{w}\ (\text{g}/\text{cm}^2)$	$(\bar{w} - w)/\bar{w}$
JORDAN	299.15	9.92	4.38	4.34	-0.01
AUGSTEIN	299.15	10.13	4.94	4.33	-0.14
ESTOQUE a	297.65	10.39	5.26	4.09	-0.28
ESTOQUE b	298.65	9.31	4.58	4.25	-0.08
GODBOLE	299.65	11.13	5.43	4.41	-0.23

We can conclude from the preceding discussion of spectral simulations that the relationship between ℓ and w , shown in Fig. 6, is reasonably applicable for the various atmospheric conditions we have considered. The parameter $(\bar{w} - w)/\bar{w}$ in a general fashion reflects excess or deficit of water vapor content in the atmosphere with respect to some mean conditions. For positive values this parameter, together with some statistical information, can be related to the strength of the trade wind inversion. Negative values of this parameter indicate the presence of deep moisture convection such as that produced by ITCZ.

OBSERVATIONS AND RESULTS

The Nimbus 4 IRIS obtained spectral measurements for a period of about 9 months from April to December 1970. The field of view of IRIS was about 95 km in diameter and this instrument had only subsatellite viewing geometry. As the successive orbits of the satellite are about 26° longitude apart and as some data are cloud contaminated, it is not possible to construct a global map of the line strength ℓ for each day. It was found necessary to combine about 90 days of IRIS data to get a satisfactory global map. For this reason we have divided the IRIS data into three periods April - June, July - September and October - December, and derived three global maps of ℓ . The cloud contamination is eliminated with the help of

the brightness temperature in the $11\ \mu\text{m}$ window region. It is assumed that when the window temperature exceeds 290 K in the 20°N to 20°S latitude belt over the oceans clouds are absent. Similarly a threshold of 285 K and 280 K are applied to the belts $20^\circ - 30^\circ$ and $30^\circ - 50^\circ$, on either side of the equator, respectively. From the description of the data used in this analysis it is clear that some biasing of the information toward clear sky conditions will prevail. In addition the composite of data may not lead to a fair spatial and seasonal average. Three maps of ℓ , corresponding to the three time periods mentioned above, derived in this fashion, are shown in Figs. 12, 13 and 14. Using the corresponding $11\ \mu\text{m}$ IRIS window data and utilizing the split window technique described by Prabhakara et al. (1974) for each one of these periods, a sea surface temperature (SST) map is derived. These SST maps are shown in Figs. 15, 16 and 17.

These maps of ℓ and SST essentially constitute the basic observational information for the subsequent discussion. The data between longitude region of about 100° to 120°E are missing due to some telemetry limitation. As a consequence the information on this part of the Indian Ocean is not contained in our analysis.

The strength of the water vapor lines ℓ , as shown in the previous section has a quasi-linear dependence on the total water. This is not surprising as ℓ is a water vapor spectral feature in the window region.

To further validate this result we have used ground truth data obtained from ship and island radiosonde stations. The satellite $9\ \mu\text{m}$ line strength measurements, within $\pm 1^\circ$ latitude and longitude from the stations, are used to estimate the total water content according to the relationship shown by solid line in Fig. 6. The cloud contamination was avoided by accepting only the data in which the surface temperature reported by the ship (or island) differed by no more than 1.5°C with respect to satellite derived SST. In this fashion we were able to gather 53 cases for comparison, shown in Table 6a and b, covering about 10 month

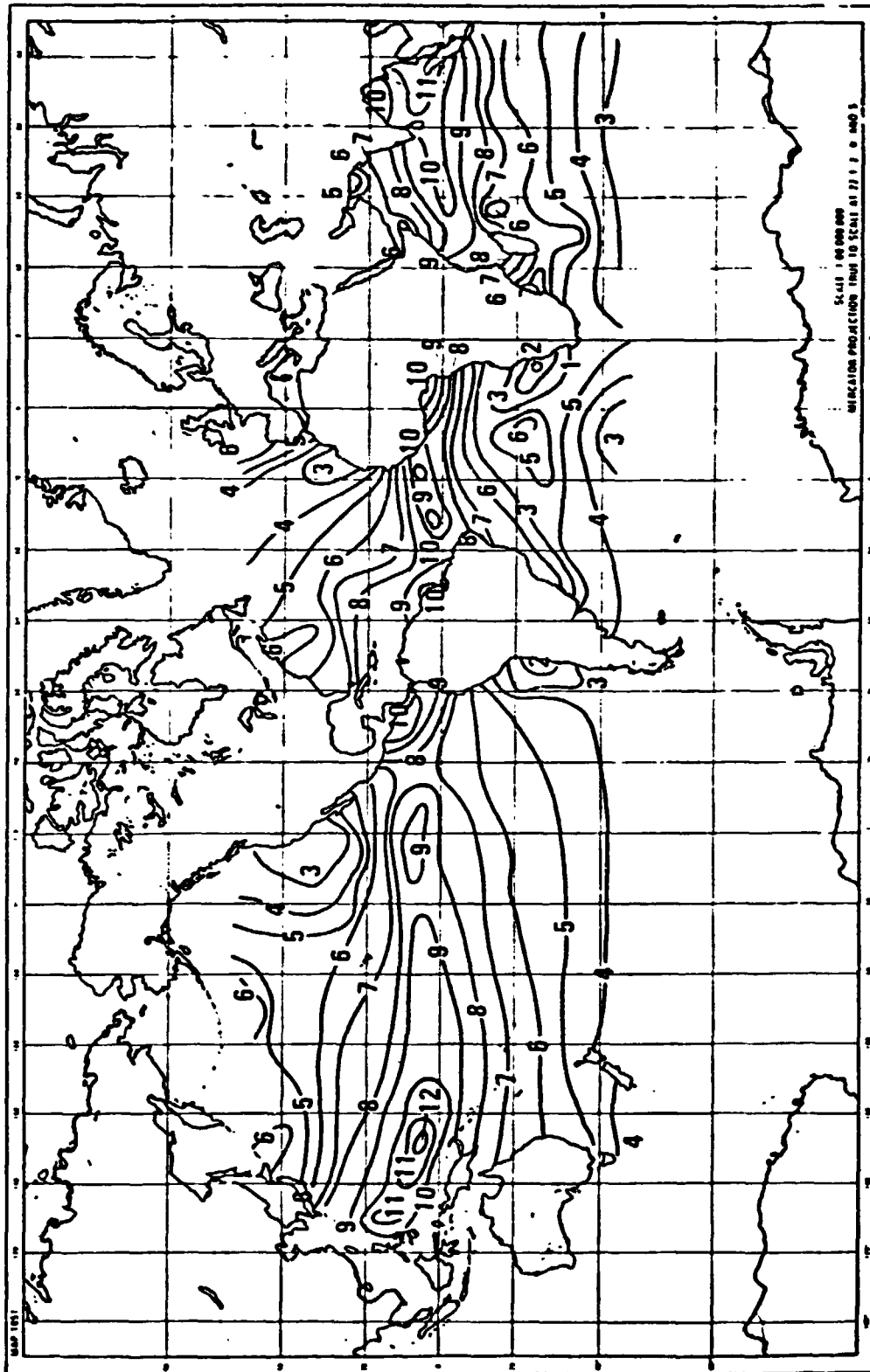


Figure 12. Distribution of the $9\mu\text{m}$ line strength over the global oceans (50°N to 40°S) derived from the Nimbus 4 IRIS data for the period April, May and June, 1970.

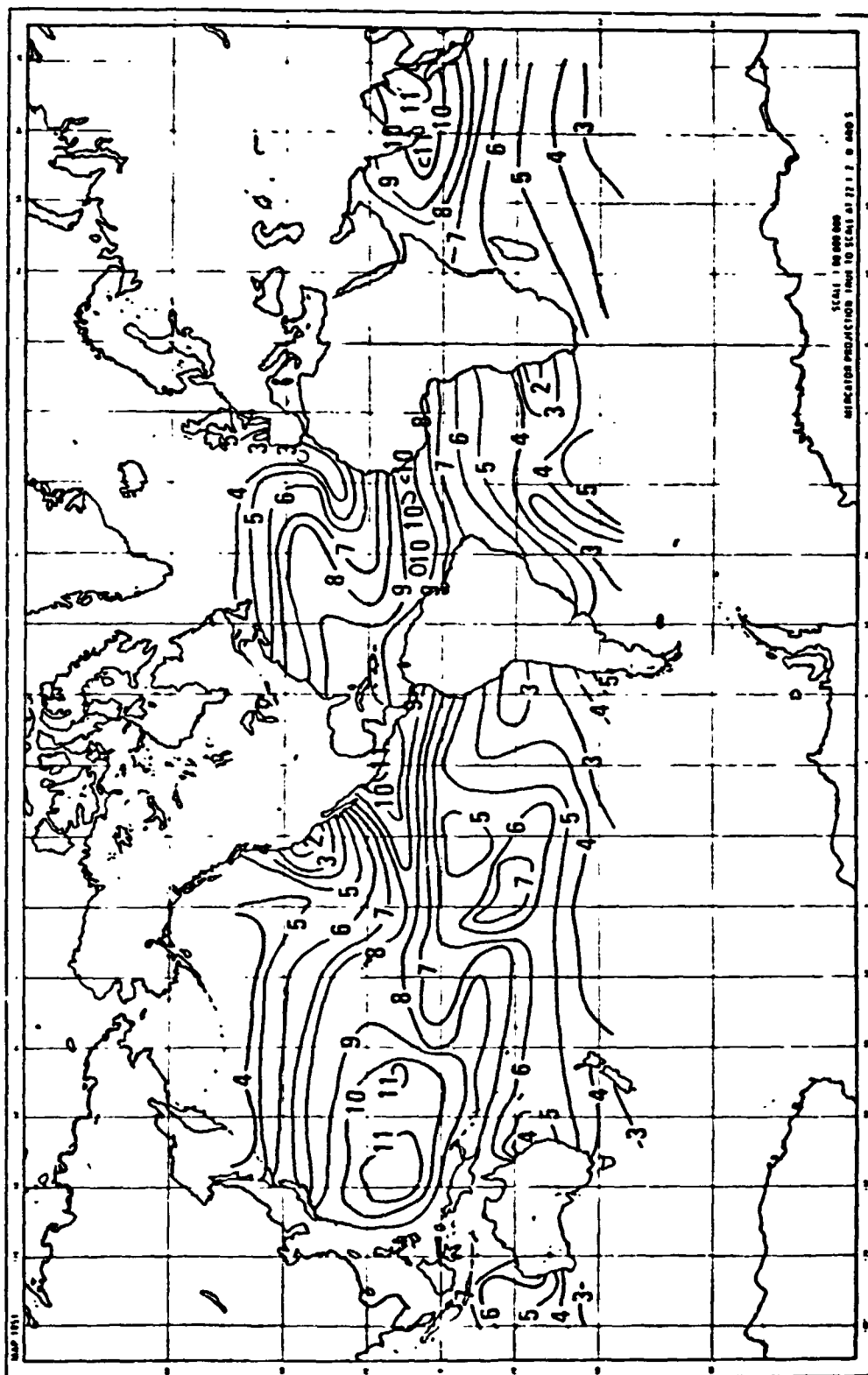


Figure 13. Same as Fig. 12 but for the period July, August and September, 1970.

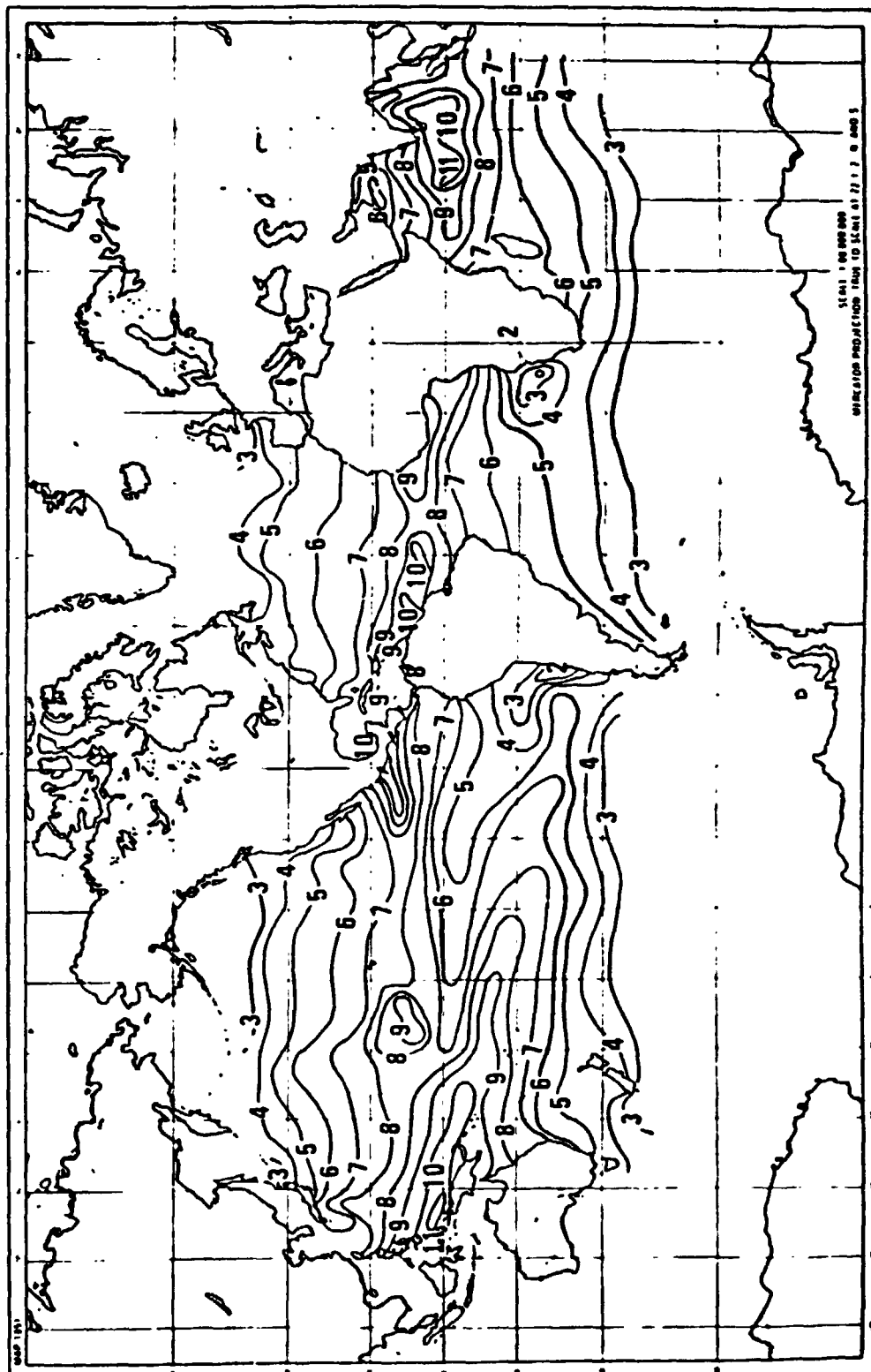


Figure 14. Same as Fig. 12 but for the period October, November and December, 1970.

ORIGINAL PAGE IS
OF POOR QUALITY

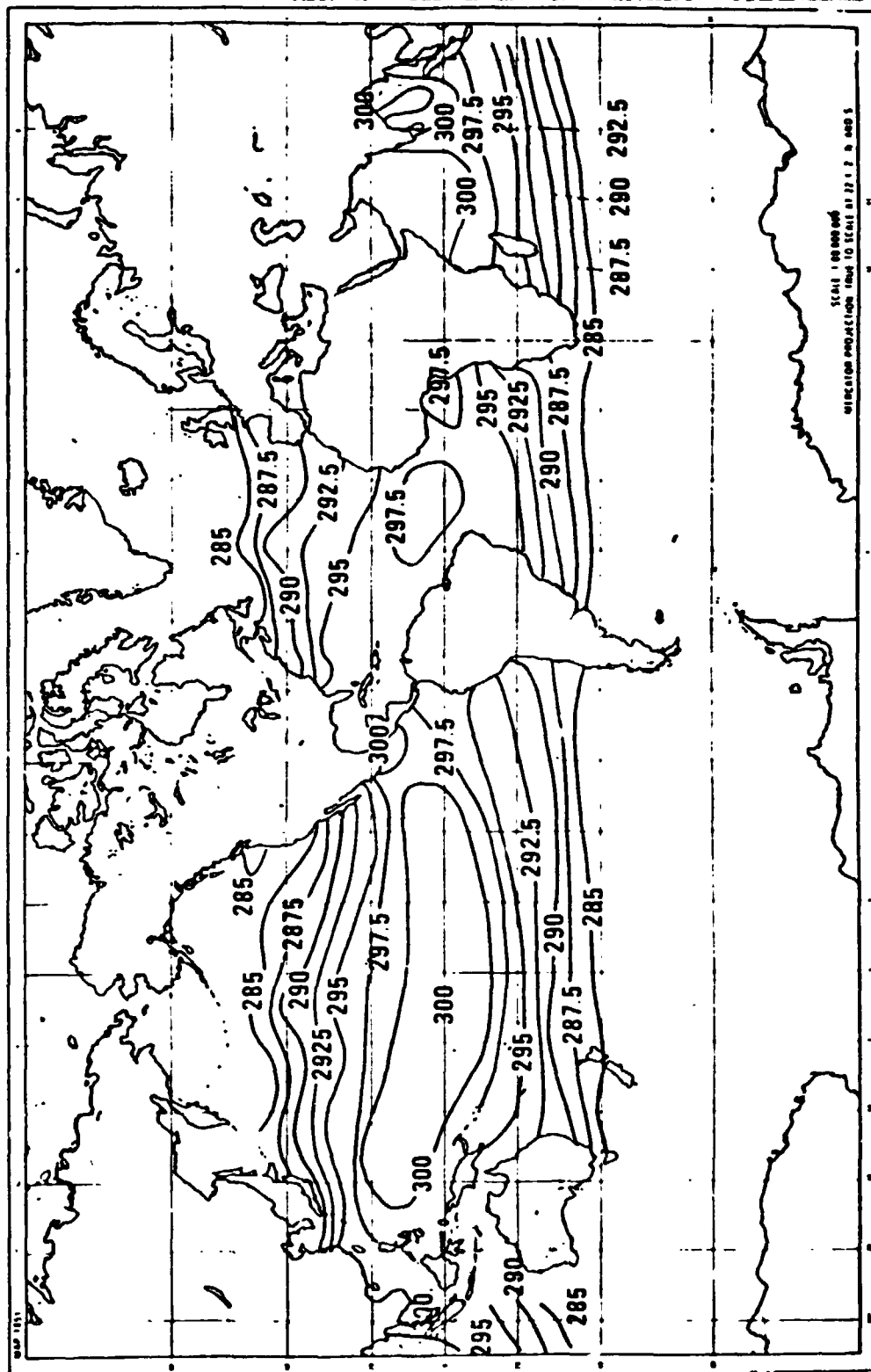


Figure 15. Distribution of the surface temperature over the global oceans (50°N to 40°S) derived from the 11 μm window region observations of the Nimbus 4 IRIS for the period April, May and June, 1970.

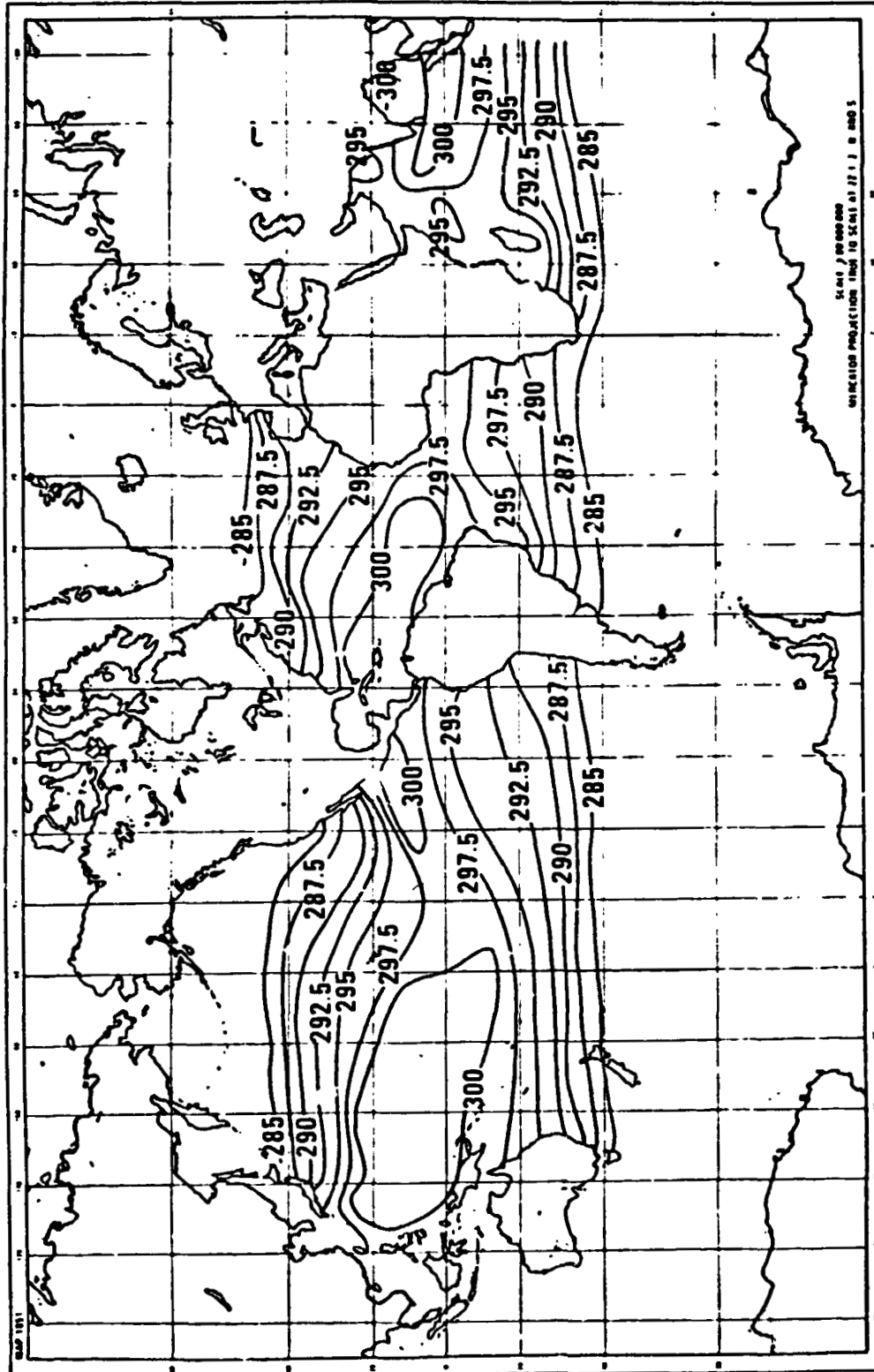


Figure 16. Same as Fig. 15 but for the period July, August and September, 1970.

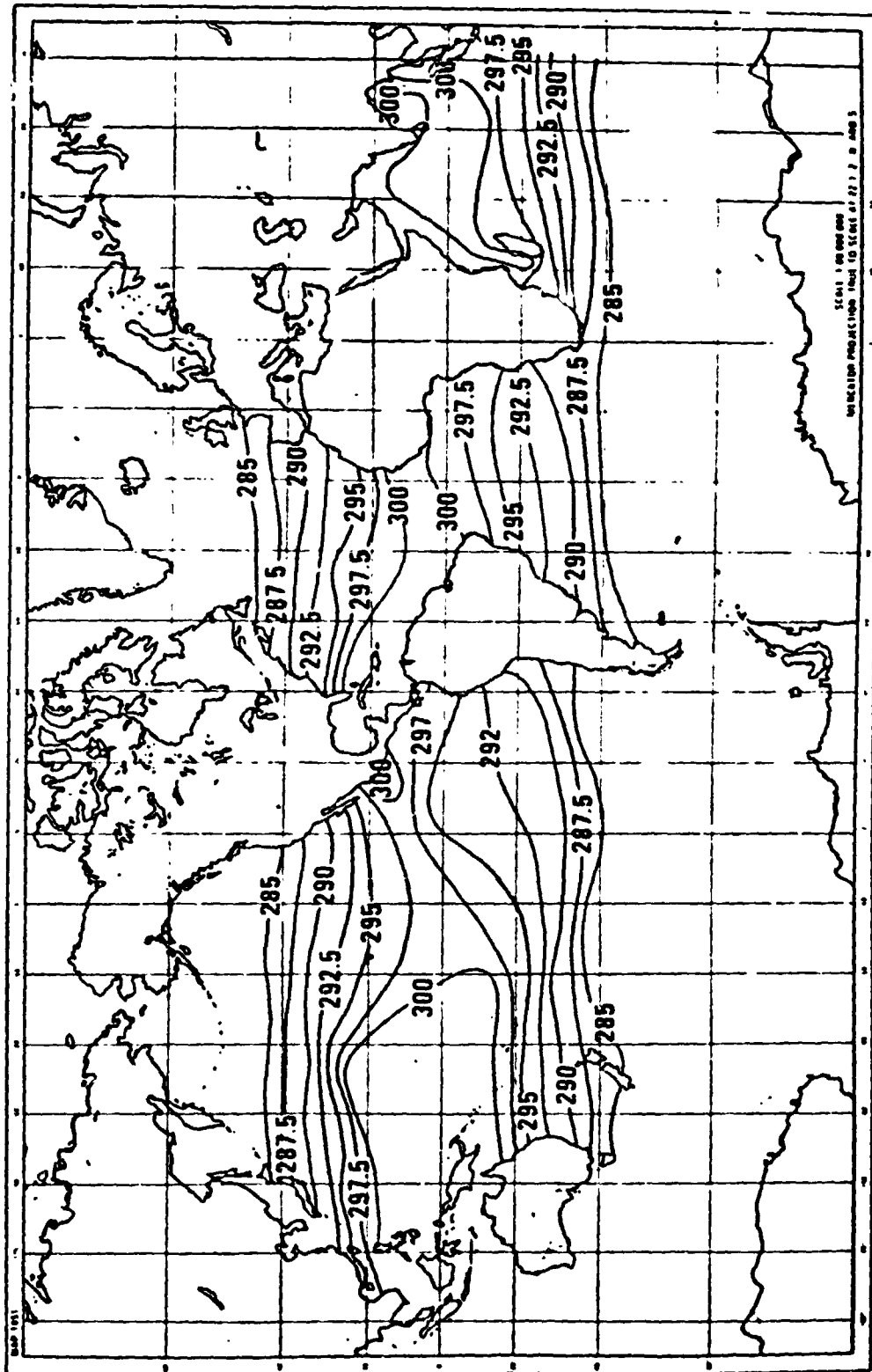


Figure 17. Same as Fig. 15 but for the period October, November and December, 1970.

Table 6a

Coincident data from ship radiosonde stations and Nimbus 4 IRIS

Day	Ship	T _{IRIS} (K)	T _{SHIP} (K)	RF(p ₀) (%)	t _{IRIS} (°C)	w _{IRIS} (g/cm ²)	w _{SHIP} (g/cm ²)
Apr. 19	4 Y M	275.9	277.9	93	3.37	1.16	0.93
Apr. 22	W T K A	297.0	299.4	82	9.12	4.11	3.82
May 7	4 Y J	280.4	281.0	66	3.75	1.32	0.91
May 9	4 Y N	290.5	290.9	68	4.78	1.78	1.90
May 12	4 Y M	278.7	280.1	84	3.03	1.01	0.99
May 17	4 Y N	289.9	291.5	76	5.34	2.04	1.93
May 21	4 Y J	282.4	283.7	92	3.30	1.15	1.58
June 6	4 Y N	290.4	292.9	63	5.09	1.92	1.72
June 12	4 Y V	294.3	292.7	98	8.18	3.54	3.46
June 18	4 Y J	282.5	285.1	76	3.96	1.41	1.35
June 21	4 Y E	294.6	294.1	89	8.75	3.87	3.71
June 21	4 Y N	291.1	293.1	82	5.92	2.33	1.73
July 2	4 Y J	283.9	284.9	85	4.38	1.61	1.82
July 3	4 Y D	290.6	293.1	92	5.59	2.18	2.80
July 12	4 Y E	298.6	297.7	77	8.06	3.48	3.50
July 17	4 Y V	295.7	297.9	88	6.44	2.60	2.64
July 31	4 Y D	293.5	293.3	95	7.12	2.96	2.58
Aug. 2	4 Y N	294.8	296.1	69	5.83	2.28	1.83
Aug. 6	4 Y B	280.7	282.7	82	3.17	1.08	1.18
Aug. 7	4 Y C	283.6	283.7	91	4.87	1.83	1.78
Aug. 9	4 Y N	295.0	295.9	76	4.96	1.83	1.74
Aug. 11	4 Y D	294.1	293.5	80	5.96	2.36	2.07
Aug. 23	4 Y I	282.4	285.1	87	4.67	1.14	1.72
Aug. 23	4 Y N	294.7	294.7	75	4.98	1.88	1.88
Aug. 30	4 Y N	295.6	295.9	85	6.47	2.62	2.54
Aug. 31	4 Y K	290.8	293.3	91	6.50	2.63	3.25
Sept. 4	4 Y P	286.0	283.7	98	5.64	2.20	2.65
Sept. 4	4 Y V	295.4	298.7	80	8.96	4.02	4.14
Sept. 16	4 Y C	281.8	281.9	81	4.38	1.61	1.37
Sept. 27	4 Y N	295.1	294.1	73	7.31	3.06	2.27
Oct. 4	4 Y N	290.5	294.9	79	5.42	2.08	2.46
Oct. 8	4 Y V	294.4	295.3	65	5.58	2.16	1.50
Oct. 13	4 Y J	286.4	285.9	87	5.26	2.00	1.87
Oct. 18	4 Y N	294.1	294.9	73	4.90	1.84	2.08
Oct. 23	4 Y P	279.3	282.1	71	3.18	1.08	0.83
Oct. 25	4 Y N	290.2	294.3	73	5.73	2.24	2.12
Nov. 27	4 Y P	282.0	280.9	80	3.67	1.27	0.91
Dec. 3	4 Y V	291.8	291.3	66	5.00	1.87	1.58
Dec. 5	4 Y E	292.5	292.2	72	6.43	2.59	2.09
Dec. 26	4 Y E	291.2	292.7	85	6.30	2.53	2.01
Jan. 26	4 Y J	280.6	281.5	75	3.07	1.05	1.12

Table 6b

Same as Table 6a but with radiosonde data from island stations.

Day	Station	T _{IRIS}	T _{ISLE}	RH(p ₀)	ℓ _{IRIS}	w _{IRIS}	w _{ISLE}
Apr. 20	78118 Turks	298.3	296.9	72	5.56	2.16	2.23
Apr. 20	78486 S. Domingo	298.4	296.8	75	6.03	2.41	2.53
Apr. 23	78970 Trinidad	299.3	298.1	90	7.52	3.18	3.57
Apr. 25	78526 San Juan	298.0	299.3	67	7.13	2.97	3.05
Apr. 29	91245 Wake	298.7	301.8	71	7.38	3.10	3.05
May 3	78806 Howard	296.9	297.7	93	10.46	5.00	5.07
May 8	91165 Lihue	297.2	300.2	72	6.08	2.43	2.57
May 11	78118 Turks	297.4	297.1	66	6.14	2.45	2.57
May 13	91285 Hilo	299.7	298.8	69	6.16	2.46	2.61
May 18	78526 San Juan	298.9	298.8	71	7.30	3.06	2.71
May 18	78988 Plesman	299.5	300.9	81	10.30	4.90	5.15
May 21	78970 Trinidad	298.7	300.5	83	10.00	4.70	4.17

period over the north Atlantic. The radiosonde data that went into this sample contained atmospheric conditions ranging from inversion to convectively active situations. This comparison, presented in Fig. 18, reveals that the total water content estimated from the 9 μ m line strength agrees with the radiosonde measurements within about 15%.

From the relationship, shown in Fig. 6, between ℓ and w we have constructed three maps, Figs. 19, 20, 21, of total water vapor distribution over the global oceans from about 50°N to 40°S. We are not able to compare this information with a global map of total water derived from the conventional data at this time. However Grody et al. (1978) have derived such global maps of water vapor using the data from a scanning microwave spectrometer, SCAMS,

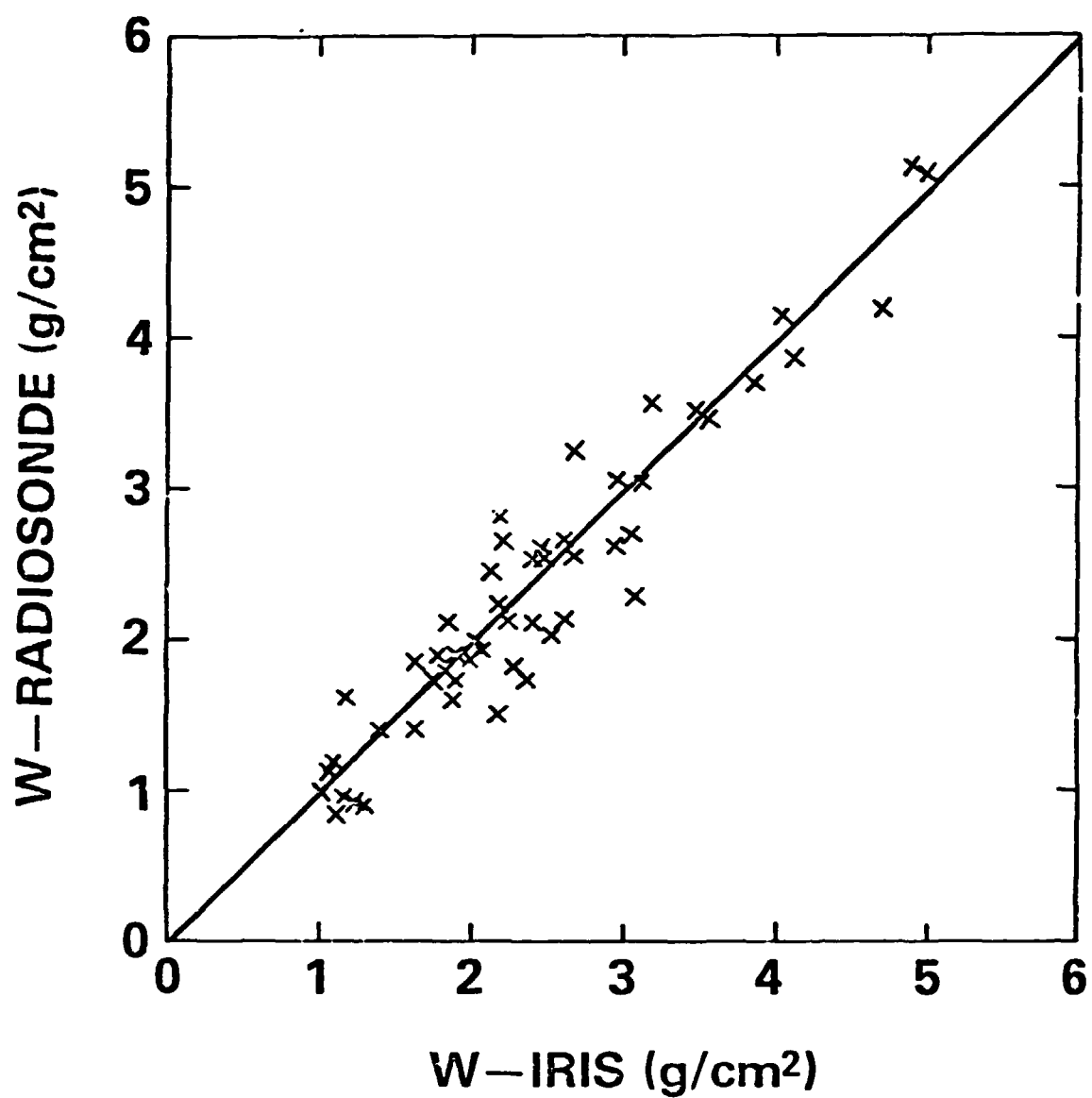


Figure 18. Comparison between the water vapor content derived from the $9\mu\text{m}$ line strength and the water vapor content obtained from radiosonde data.

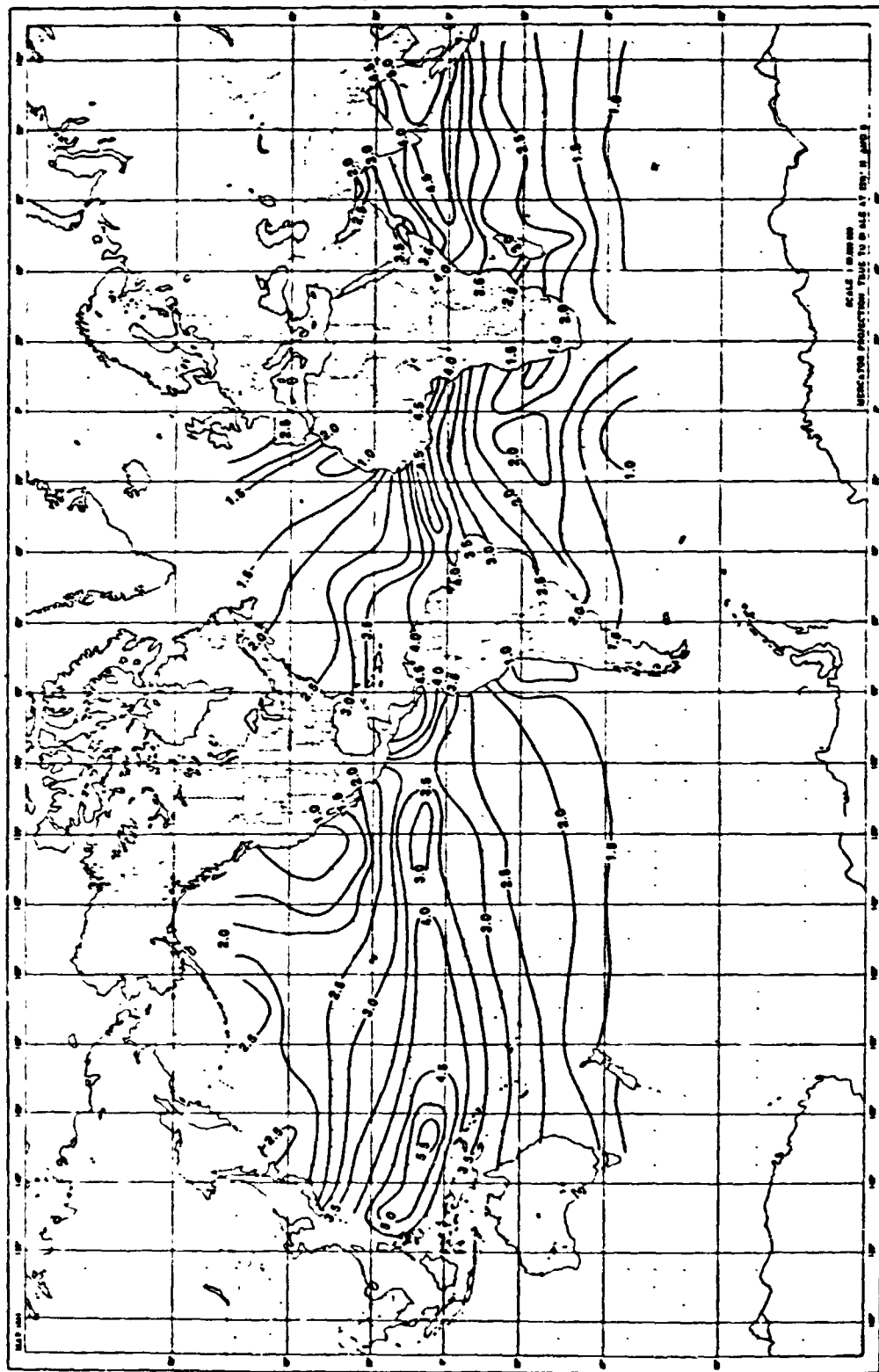


Figure 19. Distribution of the total water vapor content (g/cm^2) over the global oceans (50°N to 40°S) derived from the Nimbus 4 IRIS data over the period April, May and June, 1970.

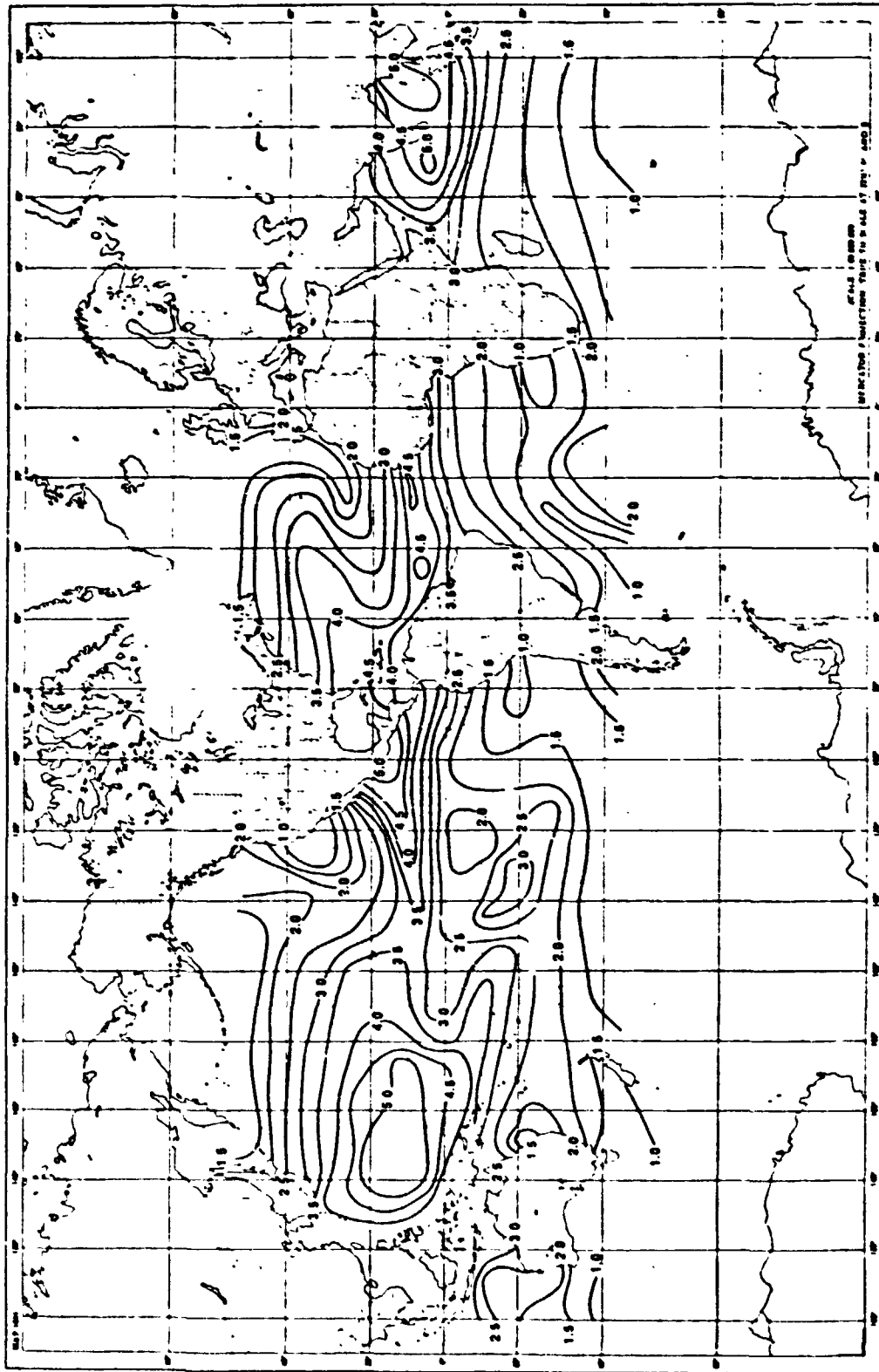


Figure 20. Same as Fig. 19 but for the period July, August and September, 1970.

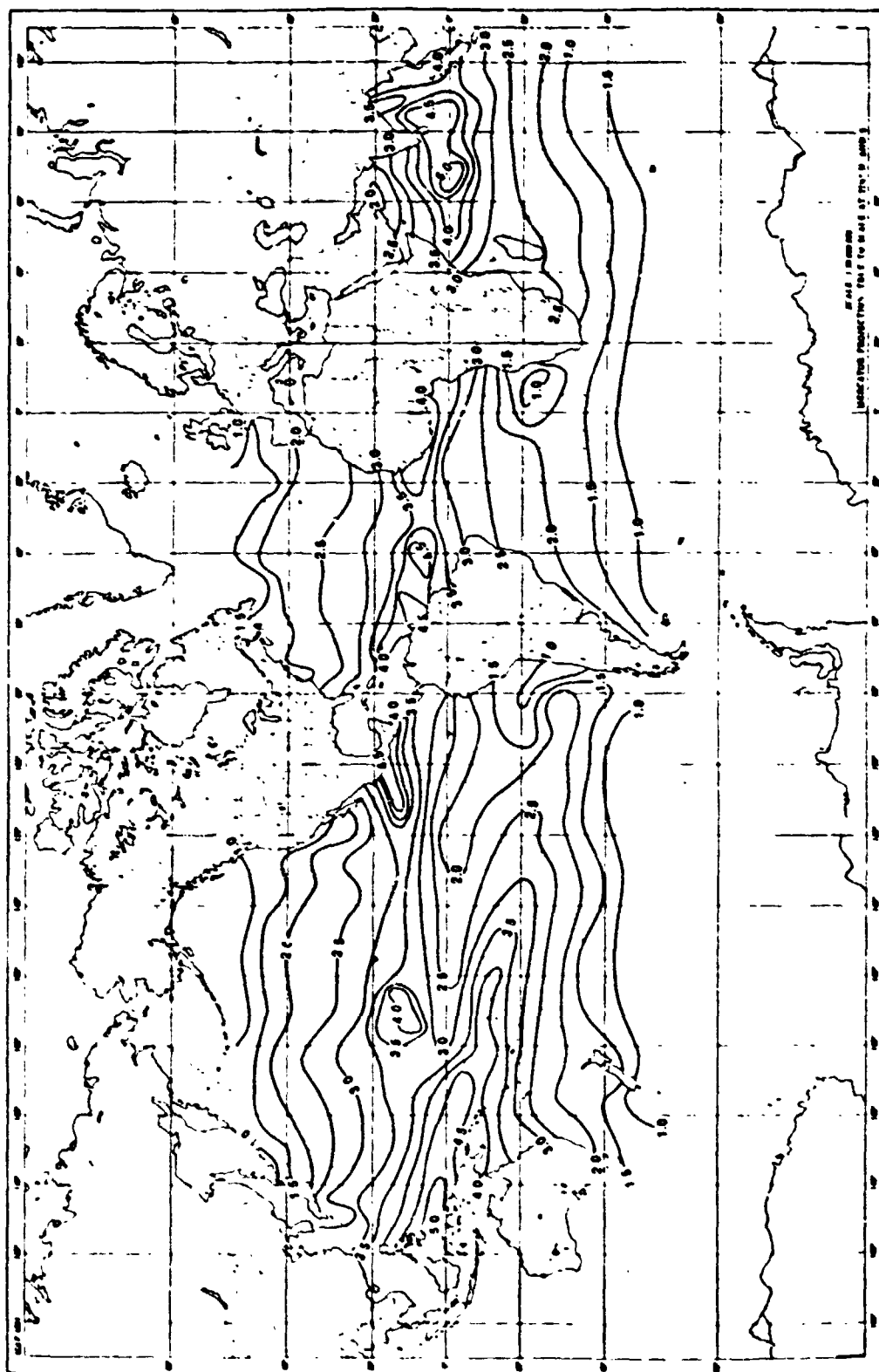


Figure 21. Same as Fig. 19 but for the period October, November and December, 1970.

that was flown on Nimbus 6. In Fig. 22 one of these maps of total water content for the period August 18 to September 4, 1975 is shown. We can compare this map with the one constructed from IRIS data for the three month period July, August and September, 1970. The distribution of the total water vapor in both these maps is very similar. This result supports our method for remote sensing of total water vapor over the global oceans. With the help of the surface temperature maps and the corresponding maps of the total water content, w , we can construct maps of $(\bar{w} - w)/\bar{w}$ for the three periods covered by the IRIS observation. These maps are shown in Figs. 23, 24, 25.

In a general fashion these maps reflect the gross structure of the boundary layer over the oceans for different seasons. The trade wind inversion associated with the subtropical anticyclone over the north and south Atlantic and Pacific oceans are clearly delineated by the positive value of $(\bar{w} - w)/\bar{w}$. From these positive values we can estimate the increase in temperature, ΔT , across the inversion from equation (6).

Over the Arabian sea strong inversion condition are revealed during the period April – June as well as during October – December. Apparently the inversion conditions are absent in the monsoon period, July – September, giving way to convective activity.

A vast region of subsidence in the equatorial pacific is revealed with some seasonal changes in strength and position. This apparently anomalous phenomenon in the equatorial Pacific is known from ship observations (see Riehl, 1954).

The regions with negative values of $(\bar{w} - w)/\bar{w}$, shown with shading in the figure, indicate the presence of convectively active areas as explained earlier. Such regions are present where the ITCZ generally prevails, as can be seen in the Figs. 23, 24, 25. Convectively active areas are also revealed along the course of the Gulf Stream and Kuroshio currents. In the southern hemisphere a significantly large belt of convectively active zone appears in the October – December period. This zone, which is about 10° latitude in width, spans from about 20°S , near the east coast of Australia, to about 35°S near Chile in South America.

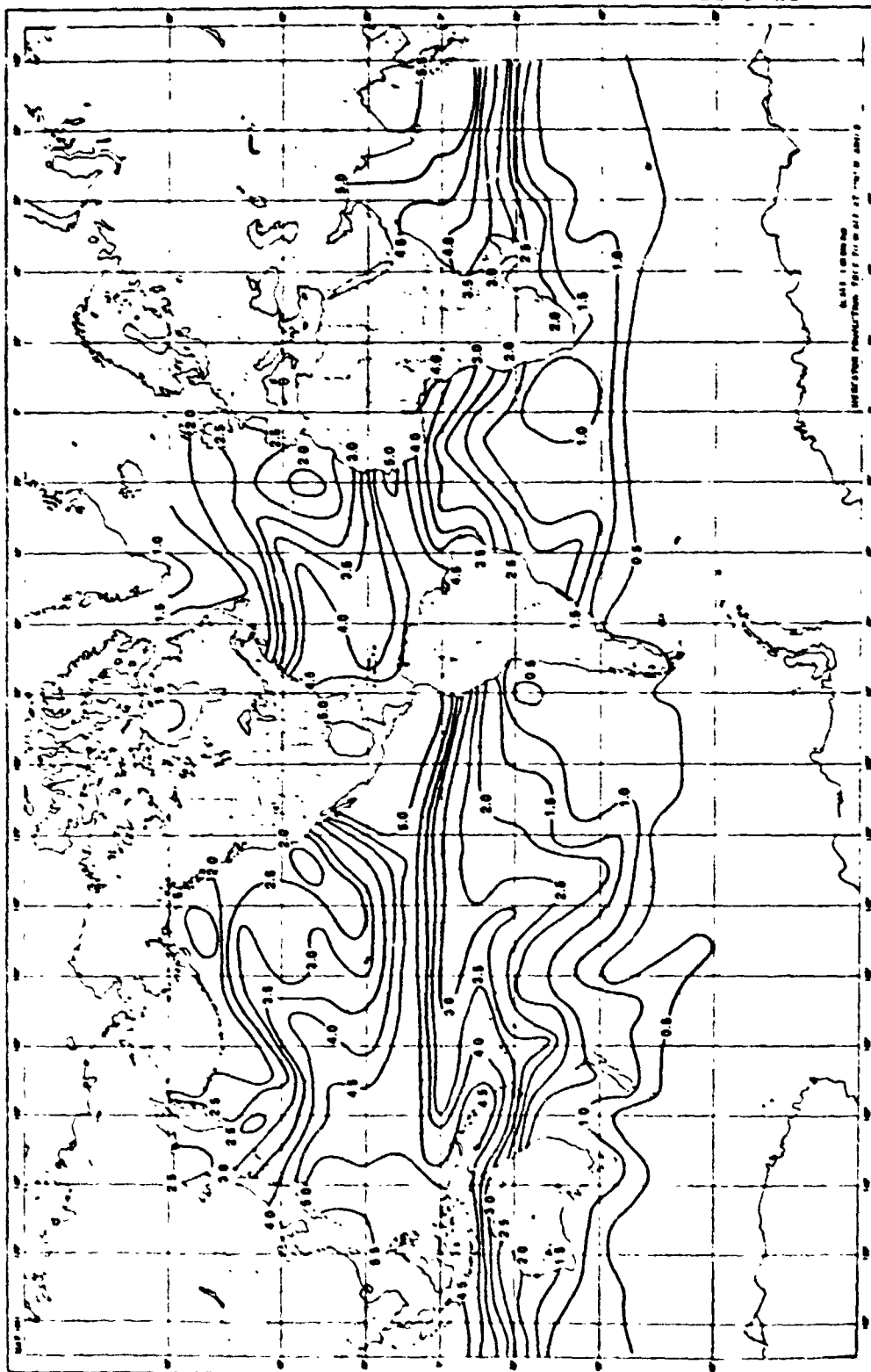


Figure 22. Mean precipitable water vapor (g/cm^2) derived from Nimbus II Scanning Microwave Spectrometer (SCAMS) for the period August 18, September 4, 1975. (After Grody, et al. 1978.)

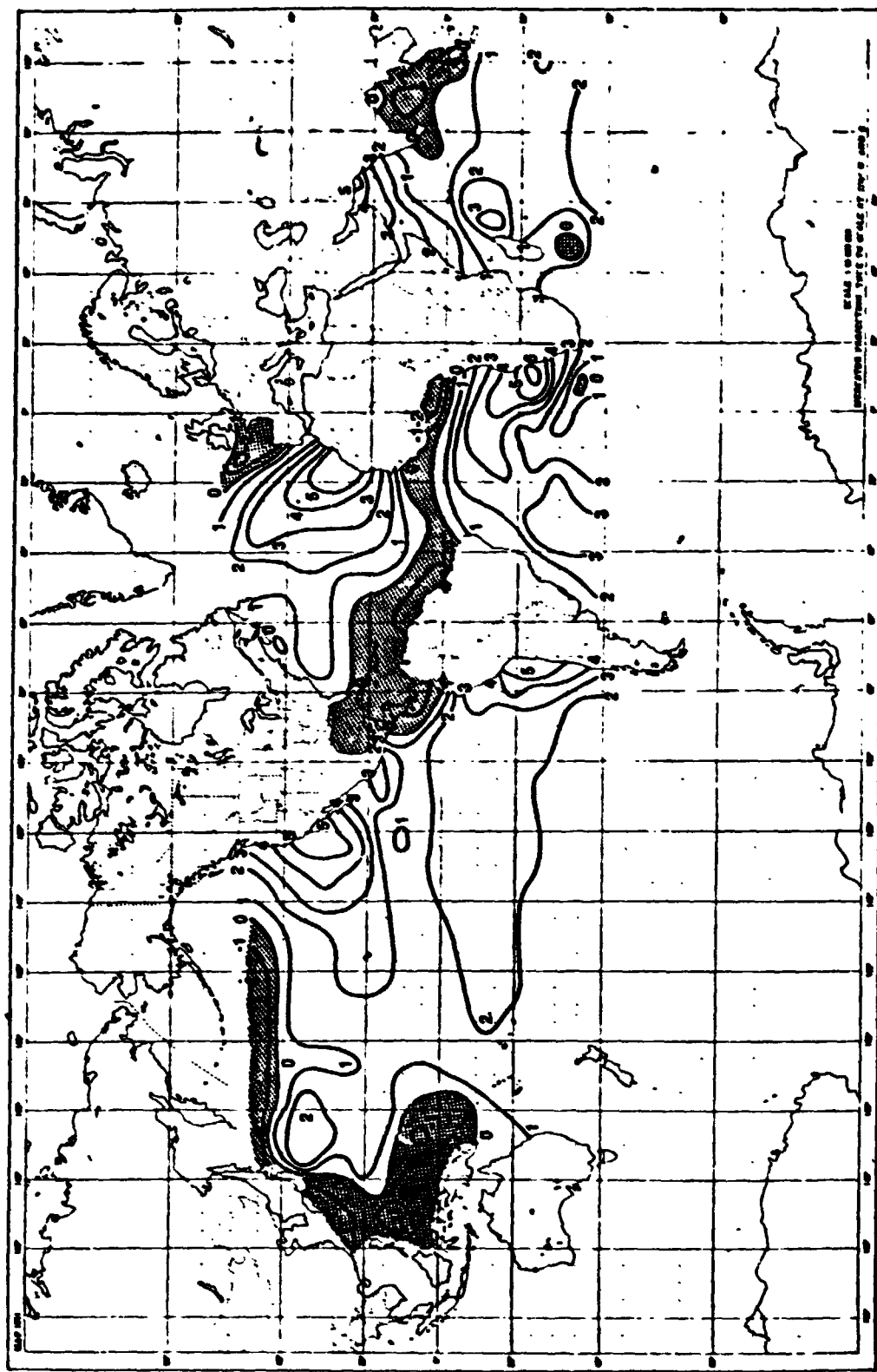


Figure 23. Distribution of the index, $(W - w)/W \times 10$, over the global oceans derived from the Nimbus 4 IRIS data for the period April, May and June, 1970. Positive value of this index gives a measure of the temperature increase from bottom to top of trade wind inversion in $^{\circ}\text{C}$. Negative values of the index are shown by shading.

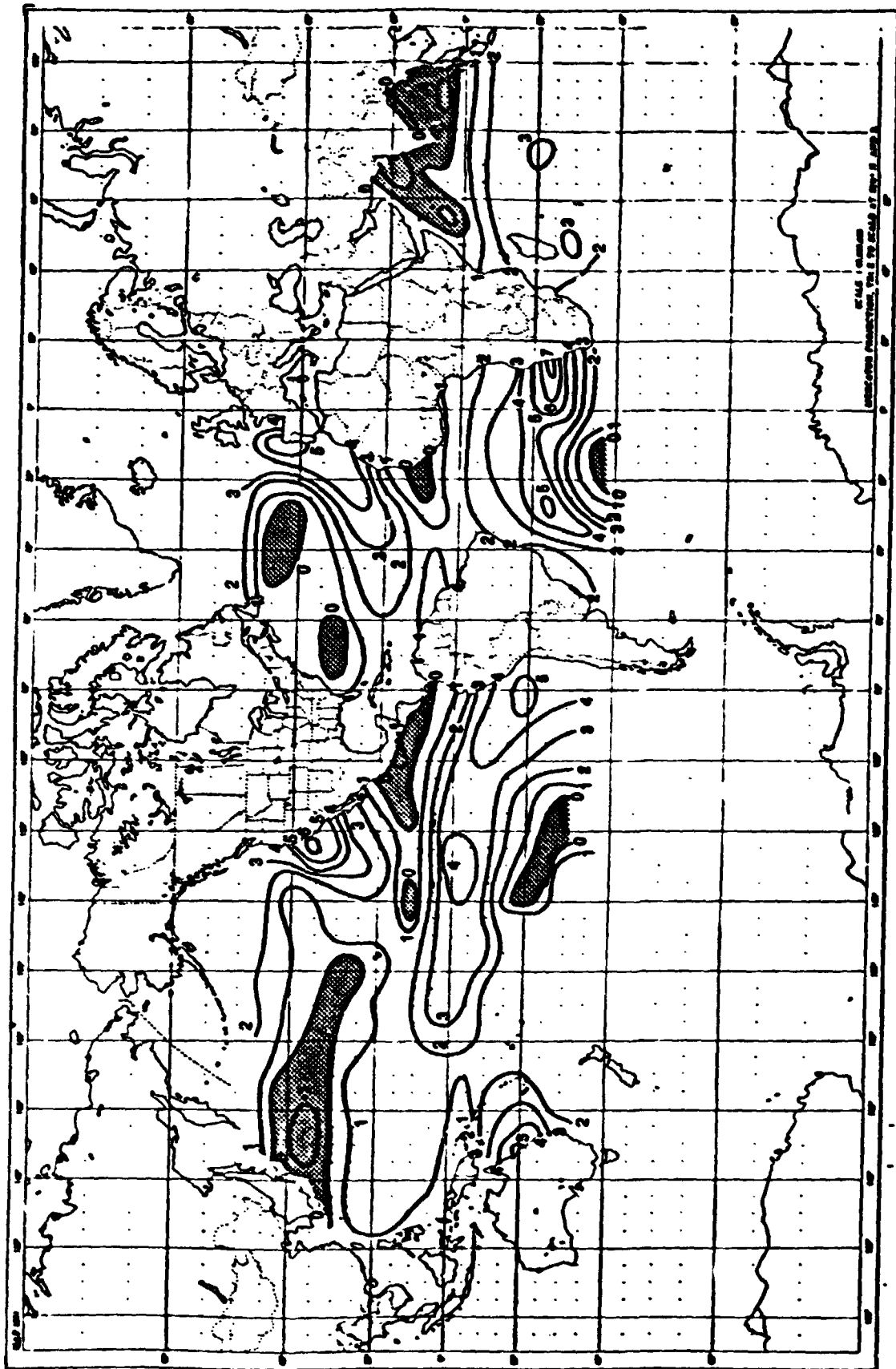


Figure 24. Same as Fig. 23 but for the period July, August and September, 1970.

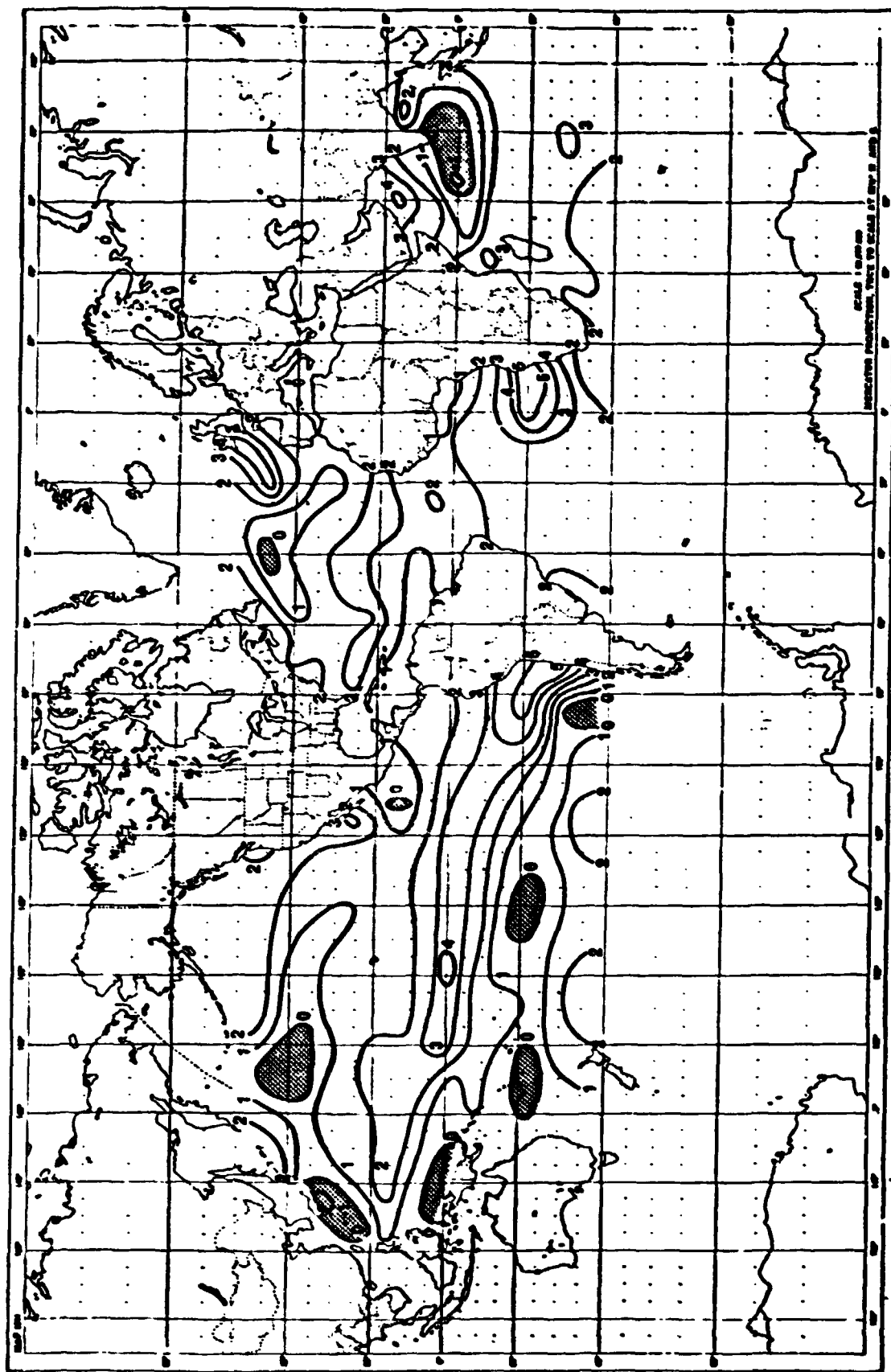


Figure 25. Same as Fig. 23 but for the period October, November and December, 1970.

The significant features of the boundary layer characteristics over the oceans revealed by Figs. 23, 24, 25, are in general agreement with the known climatology. We may conclude from this result that it is possible to infer this information from remote measurements of total water vapor and surface temperature over the oceans. This inferred information depends on one important assumption, that is, the mean water vapor profile over the global oceans can be modelled in a simple fashion. Essentially it is assumed that one mean relative humidity profile, showing a monotonic decrease from surface to 200 mb, represents the average condition applicable to all latitudes for different seasons. Departures from such mean conditions are then associated with the stable condition of inversion or convectively active state. For this reason the results obtained in this study are somewhat model dependent. Particularly if the mean relative humidity profile, significantly changes as a function of latitude and season, the patterns shown in Figs. 23, 24, 25 will be distorted. From the climatological data of Nieman it appears that the mean relative humidity profile changes within about 10% which reflects as a 10% error in w . The error introduced in $(\bar{w} - w)/\bar{w}$ from such a source has the same magnitude, i.e. 0.1. Since the range of $(\bar{w} - w)/\bar{w}$ shown in the maps is much larger than 0.1 we are able to resolve the patterns in a meaningful way.

The random errors in the remotely sensed SST and w are considerably smoothed in the three month averaging process. As a consequence the error introduced in $(\bar{w} - w)/\bar{w}$ from this source is significantly less than 0.1.

CONCLUSIONS

We have demonstrated in this study that it is possible to get a crude information on the structure of the boundary layer, over the global oceans, from remote measurements of surface temperature and total water vapor content.

Trade wind inversion over the oceans is an integral part of the tropical circulation. The studies of Malkus (1956), Mak (1976), and Ogura et al. (1977) bring out the importance of

this large scale atmospheric phenomenon. The investigation of Reiter (1978) reveals an intimate connection between the sea surface temperature anomalies and the strength of the trade winds. Several studies (see for example Namias, 1978) have revealed the significance of sea surface temperature anomalies in producing seasonal climate change. From these studies it is clear that the information we are deriving from remote measurements over the global oceans on a seasonal basis, although crude, can be valuable in understanding the ocean atmosphere interaction. This knowledge is indispensable in developing seasonal climate prediction models.

The information, obtained with the help of satellite infrared measurements, which we have presented here, is somewhat biased toward clear sky conditions. Microwave remote sensing is capable of probing through clouds when they are not precipitating. Thus it appears, when the microwave technique to sense the sea surface temperature is developed, the bias introduced by the clouds could be reduced.

REFERENCES

- Augstein, E., H. Riehl, F. Ostapoff, V. Wagner, Mass and Energy Transports in an Undisturbed Atlantic Trade-Wind Flow, *Mon. Wea. Rev.*, Vol. 101, 101-111, 1973.
- Augstein, E., H. Schmidt, and F. Ostapoff, The Vertical Structure of the Atmospheric Boundary Layer in Undisturbed Trade Wind over the Atlantic Ocean, *Boundary Layer Meteorology*, Vol. 6, 129-150, 1974.
- Bignell, K. J., The Water Vapor Infrared Continuum, *Quart. J. Roy. Meteorol. Soc.*, Vol. 96, 390-403, 1970.
- Burch, D. E., Investigation of the Absorption of Infrared Radiation by Atmospheric Gases, Publ. 4-4784, p. 27, Philco-Ford Corp., Aeronutronic Div., Newport Beach, Cali., 1970.
- Conrath, B. J., R. A. Hanel, V. G. Kunde, and C. Prabhakara, The Infrared Interferometer Experiment on Nimbus 3, *J. Geophys. Res.*, Vol. 75, 5831-5857, 1970.
- Dunkel, M., L. Hasse, L. Krügermeyer, D. Schriever, Turbulent Fluxes of Momentum, Heat, and Water Vapor in the Atmospheric Surface Layer at Sea During ATEX, *Boundary Layer Meteorology*, Vol. 6, 81-106, 1974.
- Estoque, M. A., Structure of the Mid-Oceanic Intertropical Convergence Zone, *J. Met. Soc. of Japan*, Vol. 53, n. 5, 317-321, 1975.
- Estoque, M. A., and M. Douglas, Structure of the Intertropical Convergence Zone over the GATE area, *Tellus*, Vol. 30, 55-61, 1978.
- Ficker, H., Die Passatinversion, *Veröffentlichungen des Meteorologischen Instituts der Universität Berlin*, Vol. 1, n. 4, pp. 33, 1936.
- Godbole, R. V., and S. K. Ghosh, The Structure of the Intertropical Convergence Zone and Equatorial Westerlies during MONEX-1973, *Tellus*, Vol. 27, n. 2, 123-131, 1975.
- Grody, N. C., High Resolution Passive Microwave Satellites. Applications to Synoptic Meteorology and Climatology, Application Review Panel Report Chapter 6, Edited by D. H. Staclin and P. W. Rosenkranz, MIT Research Laboratory of Electronics, pp. 6.1-6.40, 1978.

- Hanel, R. A., B. J. Conrath, V. G. Kunde, C. Prabhakara, I. Revah, V. V. Salomonson, and G. Woford, The Nimbus 4 Infrared Spectroscopy Experiment, 1. Calibrated Thermal Emission Spectra, *J. Geophys. Res.*, Vol. 77, 2629-2641, 1972.
- Haurwitz, B., and J. M. Austin, *Climatology*, McGraw-Hill Book Co., Inc., New York, pp. 410, 1944.
- Jordan, C. L., Mean Soundings for the West Indies Area, *J. Meteorol.*, Vol. 15, 91-97, 1958.
- Kunde, V. G., and W. C. Maguire, Direct Integration Transmittance Model, *J. Quant. Spectrosc. Radiat. Transfer*, Vol. 14, 803-817, 1974.
- Mak, M. K., A Model Study of the Downstream Variation of the Lower Trade-Wind Circulation, *Tellus*, Vol. 28, n. 2, 97-107, 1976.
- Malkus, J. S., On the Maintenance of the Trade Winds, *Tellus*, Vol. 8, n. 3, 335-350, 1956.
- Namias, J., Multiple Causes of the North American Abnormal Winter 1976-77, *Mon. Wea. Rev.*, Vol. 106, n. 3, 279-295, 1978.
- Nieman, R. A., A Comparison of Radiosonde Temperature and Humidity Profile Data Bases, *CSC/TM-77/6133*, Contract NAS 5-11999, pp. 48, 1977.
- Ogura, Y., J. Russel, and H. R. Cho, A Semi-empirical Model of the Trade-Wind Inversion, *Tellus*, Vol. 55, n. 3, 209-221, 1977.
- Prabhakara, C., G. Dalu, and V. G. Kunde, Estimation of Sea Surface Temperature from Remote Sensing in the 11-13 μm Window Region, *J. Geophys. Res.*, Vol. 79, 5039-5044, 1974.
- Ramage, C. S., *Monsoon Meteorology*, Academic Press, New York, pp. 296, 1971.
- Ramage, C. S., The Summer Atmospheric Circulation over the Arabian Sea, *J. Atmos. Sci.*, Vol. 23, 144-150, 1966.
- Reiter, E. R., The Interannual Variability of the Ocean-Atmosphere System, *J. Atmos. Sci.*, Vol. 35, n. 3, 349-370, 1978.

- Riehl, H., Tropical Meteorology. McGraw-Hill Book Co., Inc., New York, pp. 392, 1954.
- Riehl, H., and D. Soltwisch, On the Depth of the Friction Layer and the Vertical Transfer of Momentum in the Trades, Contrib. to Atm. Physics. Vol. 47, 56-66, 1974.
- Smith, W. L., A Polynomial Representation of Carbon Dioxide and Water Vapor Transmission, ESSA Technical Report NESC-47, U.S. Department of Commerce, National Environmental Satellite Center, Washington D.C., 20 pp., 1969.
- Staelin, D. H., A. L. Cassel, K. F. Kunzi, R. L. Pettyjohn, P. W. Rosenkranz, and J. W. Waters, Microwave Atmospheric Temperature Soundings: Effects of Clouds on the Nimbus 5 Satellite Data, J. Atmos. Sci. Vol. 32, 1970-1976, 1975.
- Wark, D. Q., and H. E. Fleming, Indirect Measurements of Atmospheric Temperature Profiles from Satellites, Mon. Wea. Rev., Vol. 94, n. 6, 351-362, 1966.

TABLES

- Table 1 Mean profiles of relative humidity and temperature for different latitude belts and seasons (from Nieman, 1977).
- Table 2 Mean line strength ℓ and total precipitable water \bar{w} as a function of the surface temperature T_s for different mean atmospheres.
- Table 3 Three parameters representation of the trade wind inversion (based on Meteor data, see Figs. 7 and 8).
- Table 4 Computed $9\ \mu\text{m}$ line strength corresponding to three trade wind inversions (see Table 3) for tropics (a), mid-latitude summer (b), and mid-latitude winter (c).
- Table 5 (a) Temperature and relative humidity profiles for observed cases of ITCZ.
(b) Calculated $9\ \mu\text{m}$ line strength, the total water content w , and the index $(\bar{w} - w)/\bar{w}$ for the ITCZ cases.
- Table 6 (a) Coincident data from ship radiosonde stations and Nimbus 4 IRIS.
(b) Same as Table 6a but with radiosonde data from island stations.

FIGURE CAPTIONS

- Figure 1 Nimbus 4 IRIS brightness temperature spectrum taken over the equatorial Pacific (2.7°N , 140.1°W , April 20, 1970). Notice the crude structure of the water vapor lines at 2.8 cm^{-1} resolution in the $9\text{ }\mu\text{m}$ region ($1100\text{--}1230\text{ cm}^{-1}$).
- Figure 2a. Water vapor transmission function at 0.1 cm^{-1} resolution (Kunde and Maguire, 1974) for 2 g/cm^2 of precipitable water.
- Figure 2b. Same as Fig. 2a when degraded to 2.8 cm^{-1} resolution.
- Figure 3 Mean relative humidity and temperature profiles for tropics and midlatitudes summer and winter (from Nieman, 1977). The adopted R.H profile is also shown.
- Figure 4 Dependence of the $9\text{ }\mu\text{m}$ mean line strength $\bar{\ell}$ and the total water vapor content \bar{w} on the surface temperature T_s over the oceans.
- Figure 5 Weighting functions for the peak at 1232 cm^{-1} and valley at 1225 cm^{-1} for the three mean atmospheric conditions.
- Figure 6 The relationship between the $9\text{ }\mu\text{m}$ line strength and the total precipitable water for mean atmospheric conditions, for inversion conditions (from Tables 4a, b and c), and ITCZ cases (see Tables 5a and b).
- Figure 7 Example of temperature and relative humidity profiles in the trade wind inversion regime.
- Figure 8 Relationship between the temperature increase, ΔT , and the decrease in relative humidity $\Delta\text{R.H.}$ from bottom to top of inversion, derived from the observation of the Meteor expedition (Ficker, 1936).
- Figure 9 Relationship between the height h of the inversion and the increase in temperature from bottom to top of inversion derived from the observations of the Meteor expedition (Ficker, 1936).
-

- Figure 10 Adopted mean relative humidity profile (shown also in Fig. 3) and the models of the relative humidity profile for three conditions (see Table 3) of the inversion.
- Figure 11 Relationship between the temperature increase ΔT , from bottom to top of the inversion and the index $(\bar{w} - w)/\bar{w}$ based on the data given in Table 4.
- Figure 12 Distribution of the $9\text{ }\mu\text{m}$ line strength over the global oceans (50°N to 40°S) derived from the Nimbus 4 IRIS data for the period April, May and June, 1970.
- Figure 13 Same as Fig. 12 but for the period July, August and September, 1970.
- Figure 14 Same as Fig. 12 but for the period October, November and December, 1970.
- Figure 15 Distribution of the surface temperature over the global oceans (50°N to 40°S) derived from the $11\text{ }\mu\text{m}$ window region observations of the Nimbus 4 IRIS for the period April, May and June, 1970.
- Figure 16 Same as Fig. 15 but for the period July, August and September, 1970.
- Figure 17 Same as Fig. 15 but for the period October, November and December, 1970.
- Figure 18 Comparison between the water vapor content derived from the $9\text{ }\mu\text{m}$ line strength and the water vapor content obtained from radiosonde data.
- Figure 19 Distribution of the total water vapor content (g/cm^2) over the global oceans (50°N to 40°S) derived from the Nimbus 4 IRIS data over the period April, May and June, 1970.
- Figure 20 Same as Fig. 19 but for the period July, August and September, 1970.
- Figure 21 Same as Fig. 19 but for the period October, November and December, 1970.
- Figure 22 Mean precipitable water vapor (g/cm^2) derived from Nimbus 6 Scanning Microwave Spectrometer (SCAMS) for the period August 18, September 4, 1975.
(after Grody, et al. 1978.)
- Figure 23 Distribution of the index $(\bar{w} - w)/\bar{w} \times 10$, over the global oceans derived from the Nimbus 4 IRIS data for the period April, May and June, 1970. Positive
-

value of this index gives a measure of the temperature increase from bottom to top of trade wind inversion.. in °C. Negative values of the index are shown by shading.

Figure 24 Same as Fig. 23 but for the period July, August and September, 1970.

Figure 25 Same as Fig. 23 but for the period October, November and December, 1970.